Advanced Fiber Materials (2024) 6:1188–1211
https://doi.org/10.1007/s42765-024-00410-y

RESEARCH ARTICLE

Revolutionizing Antimicrobial Biomaterials: Integrating an Enzyme Degradation-Resistant Sequence into Self-Assembled Nanosystems to Overcome Stability Limitations of Peptide-Based Drugs

Weikang Yu[1] · Xu Guo[1] · Qingrui Li[1] · Xuefeng Li[1] · Yingxin Wei[1] · Changxuan Shao[1] · Licong Zhang[1] · Jiajun Wang[1] · Anshan Shan[1]

Received: 28 December 2023 / Accepted: 26 March 2024 / Published online: 2 May 2024

Abstract

Incorporating enzyme-resistant peptide sequences into self-assembled nanosystems is a promising strategy to enhance the stability and versatility of peptide-based antibacterial drugs, aiming to replace ineffective antibiotics. By combining newly designed enzymatic-resistant sequences with synthetically derived compounds bearing single, double, triple, or quadruple aromatic rings. A series of nanoscale antimicrobial self-assembled short peptides for the purpose of combating bacterial infections are generated. Nap* (Nap–^{D}Nal–Nal–Dab–Dab–NH_2, where Nap represents the 1-naphthylacetyl group) possesses the greatest clinical potential (GM_{SI} = 23.96) among the peptides in this series. At high concentrations in an aqueous environment, Nap* spontaneously generates nanofibers to capture bacteria and prevent their evasion, exhibiting broad-spectrum antimicrobial effects and exceptional biocompatibility. In the presence of physiological salt ions and serum, the antimicrobial agent exhibits strong effectiveness and retains impressive resistance even when exposed to high levels of proteases (trypsin, chymotrypsin, pepsin). Nap* exhibits negligible in vivo toxicity and effectively alleviates systemic bacterial infections in mice. Mechanistically, Nap* initially captures bacteria and induces bacterial cell death primarily through membrane dissolution, achieved by multiple synergistic mechanisms. In summary, these advances have the potential to greatly expedite the clinical evolution of nanomaterials based on short peptides combined with naphthyl groups and foster the development of peptides integrated with self-assembled systems in this domain.

Keywords Naphthyl · Nanofibers · Antimicrobial peptide · Self-assembled · Protease resistance · Antibacterial mechanism

Introduction

Microbial infections are important factors in worldwide mortality patterns. The rise of microorganisms termed "red-alert" pathogens poses an additional risk to the efficacy of frequently employed antibiotics [1–6]. Creating antimicrobial agents that are more resistant than traditional antibiotics to evolutionary resistance mechanisms is a difficult challenge. Antibacterial peptides (AMPs) work by disrupting the cell membranes of bacteria, modulating immune reactions, and governing inflammation [7–10]. These small-molecule active substances are not prone to developing drug resistance, so they are at the forefront of initiatives aimed at replacing antibiotics that are losing effectiveness. Despite the considerable benefits of AMPs in fighting drug-resistant bacteria, their progress into the clinical phase remains limited. The proteolytic and physiological instability that primarily hampers their effectiveness [11–14]. One important approach to overcoming these limitations is to create analogs for AMPs, which can include *D*-amino acids, the covalent conjugation of protease inhibitors, chemical modifications at the N- and C-termini, cyclization, and PEGylation [8, 12, 15–21]. Nevertheless, although these methods can increase protease resistance, they often fail to meet practical in vivo application standards. Specifically, they demonstrate limited protease resistance and are highly susceptible to inactivation

✉ Jiajun Wang
wjj1989@neau.edu.cn

✉ Anshan Shan
asshan@neau.edu.cn

[1] College of Animal Science and Technology, Northeast Agricultural University, Harbin 150030, People's Republic of China

when exposed to the protease concentrations typically found in gastrointestinal fluids [21]. Therefore, the development of highly stable antimicrobial drugs that satisfy clinical needs is an urgent, high-priority goal.

In recent years, considerable advances have been achieved in the fields of nanoscience and technology and in the understanding of nano-biomaterials [22–27]. Significant progress has been made in the creation of nanoscale peptide-based antimicrobial agents, increasing their effectiveness and bioavailability and controlling the drug distribution [28, 29]. This approach effectively addresses the issue of multidrug resistance [30–32]. Self-assembled short peptides with natural potential antimicrobial properties have also been developed as replacements for synthetic compounds. The development of self-assembling short peptides with antimicrobial activity has gained increasing attention, primarily due to the preference for small organic building blocks instead of naturally occurring, complex AMPs [7, 33, 34]. This characteristic positions self-assembling short peptides as novel entities for bacterial therapy. Nevertheless, most research on self-assembling short peptides concentrates on altering their morphological, structural, and functional characteristics. Despite their potential as antibacterial biomaterials, the physiological stability, in vivo applicability, and systematic characterization of the mechanism of action of self-assembling short peptides have been minimally explored [35]. Small cationic peptides offer an advantage over high-molecular-weight peptides because they can evade recognition by proteolytic enzymes, thereby avoiding hydrolytic degradation [36]. Moreover, self-assembly increases the stability against proteolytic degradation under physiological conditions by protecting the cleavage site and decreasing the binding affinity for proteases [11, 13, 29]. Hence, we speculated that combining strategies, such as supramolecular self-assembly and optimization of the sequence of short peptide chains for resistance to enzymatic hydrolysis, has the potential to increase the bioavailability and therapeutic efficacy of peptide-based antimicrobial drugs.

Herein, self-assembled short peptide nanofibers were designed to treat bacterial infections. The peptide design concept to confer resistance to protease hydrolysis consists of three parts: (i) Anti-enzymolysis sequences are constructed from unnatural amino acids. 1-naphthylalanine (Nal, phenylalanine variant) was chosen to increase the affinity of the peptide affinity for the membrane, and 2,4-diaminobutanoic acid (Dab, a lysine variant) was introduced to impart a positive charge to the peptide, ensuring electrostatic interaction with the cell membrane. Our previous studies demonstrated the robust enzymatic hydrolysis resistance of Nal and Dab [18, 19]. (ii) The short peptide sequence consists of only four amino acids, aiming to minimize synthesis costs and optimize the synthesis process. (iii) The selection of a hydrophobic scaffold comprising a single benzene ring, double benzene rings, triple benzene rings, or quadruple benzene rings covalently linked to the N-terminus of the anti-enzymatic hydrolysis sequence to serve as the driving force for peptide self-assembly. In this proof-of-concept study, our objective was to design a short peptide to serve as the anti-enzymatic sequence and to explore the feasibility of varying the number of benzene rings in the hydrophobic scaffold as a means to optimize the relationship between the biocompatibility, biological efficacy, and physiological stability of the self-assembling system. We further aimed to investigate the dual effects of using a benzene ring-based self-assembling system and short peptide anti-enzyme sequences to prepare the next generation of antimicrobial agents. Here, we demonstrated that a short peptide sequence (Nap*) with naphthalene as the hydrophobic scaffold could spontaneously self-assemble into nanofibers in aqueous medium. Nap* nanofibers exhibited excellent low-toxicity antibacterial activity both in vitro and in vivo. Most importantly, Nap* displayed unparalleled stability and killing efficacy after incubation with salt ions, serum, and proteolytic enzymes (effective concentrations in simulated gastric fluid and simulated intestinal fluid, 10 mg/mL). Nap* demonstrated dual effects, achieving bacterial capture through the formation of nanofibers to prevent pathogen escape (restraining pathogen spread) and exhibiting significant bactericidal activity. Both the primary membrane penetration mechanism and non-membrane penetration mechanisms (including DNA binding and the generation of excess ROS) that result in pathogen death have undergone comprehensive analysis. This study offers insights into the design of minimal anti-enzyme short peptide nanofiber templates. The highly stable, multifunctional self-assembling short peptide Nap* has the potential for successful clinical translation (Scheme 1).

Experimental Section

Bacterial Strain Source

Bacterial strains were acquired from frozen stock at the College of Animal Science and Technology of Northeast Agricultural University, with subsequent testing confirming the absence of mycoplasma contamination.

Synthesis and Characterization of Engineered Peptides

Peptides utilized in this work were produced by GL Biochem Ltd. (Shanghai, China). Their molecular weights were determined using matrix-assisted laser desorption/ionization time-of-flight mass spectrometry (MALDI-TOF MS; Linear Scientific Inc.). Peptide purity (> 95%) and retention time were evaluated using RP-HPLC with a GS-120-5-C18-BIO

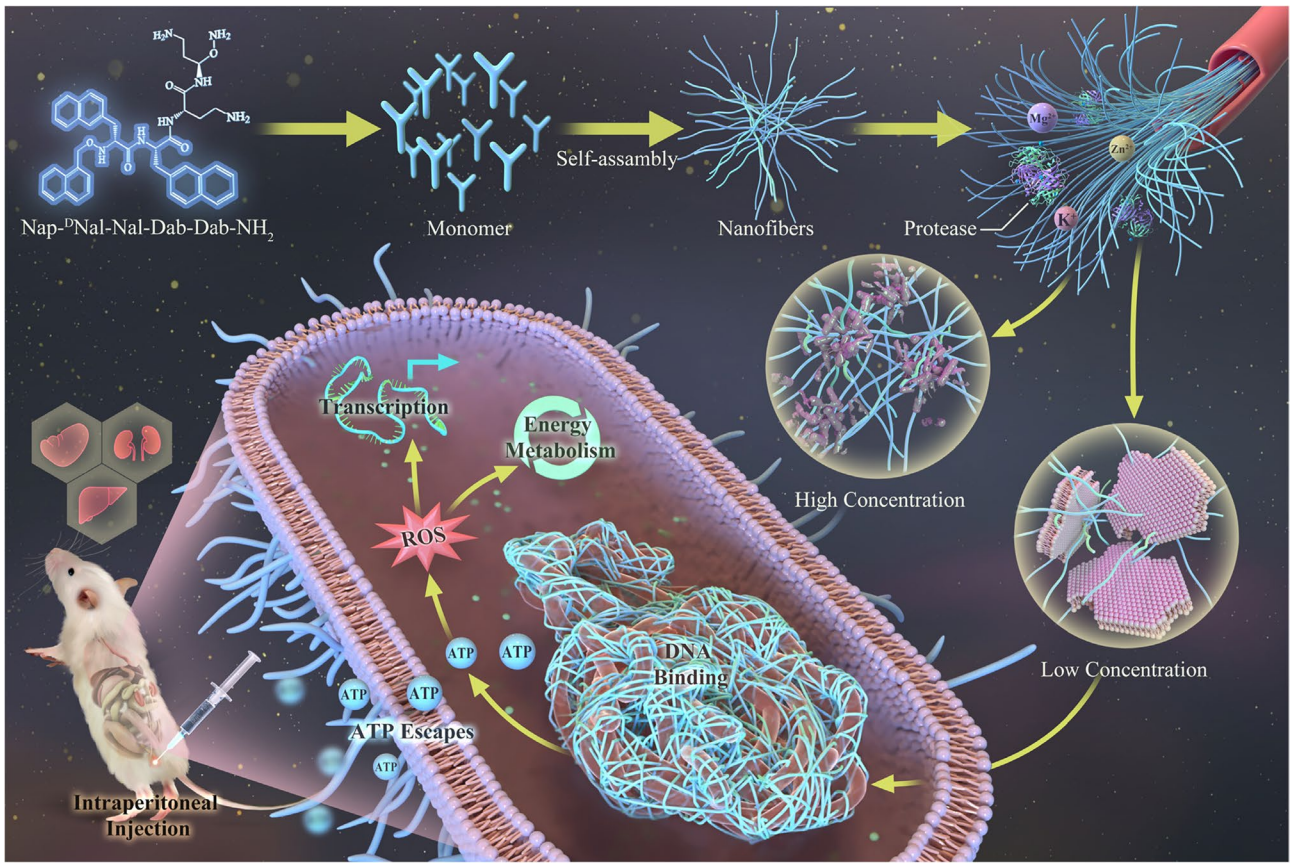

Scheme 1 Illustration of the stability, potential bactericidal mechanisms, and in vivo efficacy of Nap* nanofibers

4.6 × 250 mm^2 column at 220 nm. The mobile phase included a non-linear gradient of water and acetonitrile with 0.1% trifluoroacetic acid, a sample volume of 5 µL, and a flow rate of 1.0 mL/min.

Critical Aggregation Concentration (CAC) Assay

The CAC value was determined using 1-anilino-8-naphthalene sulfonate (ANS) as a fluorescent probe in a fluorescence test. Different peptide concentrations dissolved in deionized water were added to 1 µL of ANS (1 mmol/L) dissolved in N,N-dimethylformamide (DMF). Afterward, the blend was transferred to an incubator set at 37 °C for 15 min. After the incubation period, the samples were moved to a 96-well plate and analyzed utilizing a fluorescence spectrophotometer (Hitachi, Japan) with an excitation wavelength of 369 nm. The fluorescence emission spectrum was recorded in the range of 420–550 nm.

Antimicrobial Assay

The minimum inhibitory concentrations (MICs) and minimum bactericidal concentrations (MBCs) of the engineered peptides were established following the same procedure outlined in a previous study [20]. The MIC was determined by inoculating bacterial strains stored at − 80 °C into MHB medium and diluting them to reach a concentration of 1×10^5 CFU/mL. Afterward, the peptides at varying concentrations were mixed with the bacterial solutions and left to incubate at 37 °C for 24 h. MHB without any bacteria was utilized as a control. Following the period of incubation, the cloudiness of every well was evaluated using a spectrophotometer set at a wavelength of 492 nm. The MIC was established by identifying the peptide concentration at which the well remained transparent and free of cloudiness.

The MBC was determined by placing 10 µL of each clear well solution on MHA agar plates and incubating them at 37 °C for 24 h, followed by counting the resulting colonies. The MBC was then the drug dose that successfully eradicated 99.9% of the bacterial population. Each treatment was replicated three times, with the experiment being repeated independently three times.

Kill Kinetics Assay: *E. coli* K99 was diluted in PBS (pH 7.4) at a concentration of 1×10^5 CFU/mL. Nap* (1 × MBC) was chosen for therapy, and the blend was tested within

0–1 h to determine the time–kill curves. The experiment was conducted independently on three separate occasions.

Hemolysis Assay

For the preparation of a 1% (v/v) erythrocyte dilution, human red blood cells (HRBCs) were centrifuged at 1000 × *g* for 10 min and subsequently mixed with 1 mL of PBS. Peptides were diluted sequentially in 96-well plates before being combined with HRBCs suspension in equal amounts. HRBCs treated with 0.1% Triton X-100 served as the positive controls, while the negative controls consisted of untreated HRBCs. Following kept at 37 °C for 60 min, the solutions were spun at 1000 × *g* for a period of 10 min. The liquid above the sediment was transferred to a fresh 96-well dish, and the amount of hemoglobin released was determined by a microplate reader (570 nm, Tecan Infinite 200 Pro, China). The percentage of hemolysis was determined by Eq. (1):

$$\text{Hemolysis}\,\% = \frac{(\text{sample treated with peptide} - \text{negative control})}{(\text{positive control} - \text{negative control})} \times 100. \quad (1)$$

Cytotoxicity Assay

The peptides' cytotoxic effects on two cell lines, specifically murine macrophages (RAW 264.7) and human embryonic kidney cells (HEK 293 T), were evaluated through a colorimetric MTT assay [8]. In summary, 250,000 cells were seeded into individual wells of 96-well plates and exposed to varying peptide levels for 18–24 h at 37 °C in a 5% CO_2 environment. Following the incubation time, 50 µL of MTT solution with a concentration of 0.5 mg/mL was introduced into each well and left for another 4 h. The formazan crystals were then dissolved by adding 100 µL of DMSO removing the liquid on top. The positive controls were cells that were not treated with peptides, and complete culture medium was used as a negative control.

Thioflavin T (THT) Fluorescence Assay

The ThT working solution was prepared by dissolving 2 mg/mL ThT in deionized water and then filtrating it through a 0.2-µm syringe filter. Afterward, the prepared ThT fluorescence probe was combined with an equivalent amount of Nap* in a 96-well plate and left to incubate at 37 °C for 20 min. The fluorescence emission spectra were measured at a wavelength of 482 nm using an excitation wavelength of 450 nm.

CD Spectroscopy

Nap* was mixed with deionized water to create a solution with a concentration of 64 µmol/L. SDS (30 mmol/L) and TFE (50%, v/v) were also employed. The Chirascan spectrometer from the U.K. was used to calculate the results, with Shao's method being utilized for the calculations [37].

Fourier Transform Infrared (FTIR) Spectroscopy

The Nicolet Avatar 370DTGS spectrophotometer from Thermo Fisher Scientific in the USA was utilized to gather FTIR spectra of the samples within the 4000–400 cm^{-1} range. The OMNIC 8.2 software was used to analyze the molecular structure of the infrared spectra.

Peptide Self-Assembly Observations

To perform transmission electron microscopy (TEM), Nap* was thinned with deionized water to reach a concentration of CAC-256 µmol/L (originally at 2.56 mmol/L). The solution was thinned and left to sit at room temperature for a day. Next, the samples were put on a copper-coated carbon grid and stained with 1% phosphotungstic acid for half a minute. Finally, observation was done using a Hitachi H-7800 TEM (Hitachi, Japan) at 100 kV. To perform scanning electron microscopy (SEM), 10 µL of Nap* was applied onto coverslips as a thin layer, allowed to air dry on a sterile work surface, and then examined using a Hitachi S-4800 SEM (Hitachi, Japan). The final concentration of the peptide was 256 µmol/L, 32 µmol/L and CAC. To perform atomic force microscopy (AFM), 10 µL of the same peptide sample was evenly spread on a mica sheet, allowed to dry completely in air and then examined using a Bruker Dimension Icon (Bruker AXS, U.S.).

Dynamic Light Scattering (DLS) and ζ-Potential Assay

A Zetasizer Nano Z90 (Malvern Instruments, Worcestershire, U.K.) was utilized to determine the hydrodynamic size and ζ-potential of Nap* in water. The solutions (4 µmol/L, CAC, and 256 µmol/L) were placed in disposable plastic cuvettes. Pure water was used to set the viscosity, proteins were chosen as the solute for the refractive index, and the temperature remained steady at 25 °C. Each sample underwent three measurements.

Molecular Dynamics (MD) Simulation

GROMACS 2019.6 software was utilized to perform MD simulations. The simulation box was resized to ensure that there is at least a 1.0-nm gap between each protein atom and the box. The box was filled with water molecules until it reached a density of 1. To achieve electrical neutrality, water molecules were replaced by Cl^- and Na^+ ions. To eliminate unreasonable contacts or atom overlaps, the system's energy was minimized using a steepest descent technique involving 5.0×10^4 iterations. Following energy minimization, the system's temperature was stabilized through a 100 ps equilibration utilizing the NVT ensemble at 300 K during the initial stage. A second-phase equilibration was simulated using the NPT ensemble for 100 ps at a pressure of 1 atmosphere. The primary goal was to enhance the communication between the target protein, the surrounding solution, and ions to ensure thorough pre-equilibration of the simulation system. MD simulations were performed for 100 ns using an isothermal–isostatic ensemble at 300 K and 1 atm pressure. Temperature was regulated using the V-rescale method, and pressure was controlled using the Parrinello–Rahman method. The correlation coefficients for heat and force were 0.1 ps and 0.5 ps, in that order. The van der Waals forces were calculated by the Lennard-Jones function using a nonbond truncation distance of 1.4 nm. The LINCS algorithm constrained the bond lengths of every atom. The particle mesh Ewald method was utilized to calculate long-distance electrostatic interactions, with a Fourier spacing of 0.16 nm. Visual Molecular Dynamics (VMD) was utilized to analyze the MD trajectory.

Protease Stability Assay

Protease stability assays were performed using MIC analysis, 16.5% tricine–SDS–PAGE, and RP-HPLC [12]. Peptide solutions (2.56 mmol/L) were treated with trypsin, chymotrypsin, and pepsin (20, 10, 5, or 2.5 mg/mL) in the MIC method at 37 °C for 1 h, then their MICs were measured. For the preparation of multi-enzyme coexisting solutions, the three enzymes were mixed in deionized water while maintaining the initial concentration of each enzyme at 20, 10, 5, or 2.5 mg/mL. Subsequently, equal volumes of Nap* and the coexisting enzyme solution were mixed, followed by incubation at 37 °C for 1, 24, and 48 h before determining the MIC values. The impact of incubation time on the Nap* was assessed using the tricine–SDS–PAGE technique, which involved incubating the peptides for 1, 2, 3, and 4 h in the presence of 10 mg/mL proteases. The RP-HPLC method required mixing peptide solutions (2.56 mg/mL) and protease solutions (20 mg/mL) in equal amounts and then allowing them to incubate at 37 °C. Each specimen was diluted with deionized water at specific time points (0, 1, 2, and 4 h) to a peptide concentration of 0.5 mg/mL in order to avoid further degradation. The samples were subsequently placed in boiling water and incubated for 10 min. Afterward, the samples were analyzed using an Agilent 1260 Series HPLC System (Agilent) equipped with an Agilent ZORBAX 300SB-C18 column (4.6 mm × 250 mm, 5 μm) at a flow rate of 1.0 mL/min. The mobile phase was composed of water with 0.1% trifluoroacetic acid and 95% acetonitrile with 0.1% trifluoroacetic acid.

Salt and Serum Assay

In these assays, *E. coli* ETEC K99 was used as a representative Gram-negative bacterium. Evaluating the stability of Nap* MIC in the presence of salt involved measuring the fold-change after dissolving salt powder in a solution with 0.2% BSA. The tested salt concentrations at the end were 150 mmol/L NaCl, 4.5 mmol/L KCl, 6 μmol/L NH_4Cl, 2 mmol/L $CaCl_2$, 8 μmol/L $ZnCl_2$, 1 mmol/L $MgCl_2$, and 4 μmol/L $FeCl_3$. For the serum sensitivity test, Nap* (2.56 mmol/L) was combined with 25%, 50%, and 100% serum in 0.2% BSA in equal amounts, followed by incubated for 4 h.

CLSM Assay

The bacteriostatic process was examined for the localization of Nap* through the use of FITC-labeling and propidium iodide (PI) dye. *E. coli* ETEC K99, with an optical density of approximately 0.3 at 600 nm, was grown with FITC-labeled peptides (1 × MIC) in PBS (pH 7.4, 10 mmol/L) for 60 min at 37 °C. Next, PI at a concentration of 10 μg/mL was introduced, and the combination was left to incubate for another 30 min. The unattached FITC-labeled substance and dye were rinsed with PBS (1000 × *g*, 10 min). The specimen that was suspended was moved to a glass slide, where pictures were taken using a confocal laser scanning microscope (CLSM, Leica TCS SP8, Germany) that emitted light at 488 nm for FITC and 535 nm for PI.

LPS Binding Assay

A BODIPY-TR-cadaverine (BC) probe was used to assess the binding strengths of Nap* to LPS from *E. coli* O111 B4. BC and LPS were mixed in Tris buffer (pH 7.4) at concentrations of 5 μg/mL and 50 μg/mL, respectively, then left to incubate for 4 h without light. Following this, the LPS–BC mixture was added to all wells of the 96-well plates, with one group serving as a control without any treatment (100 μL of LPS–BC mixture) and another group treated with

polymyxin B (20 μg/mL). The fluorescence intensity was measured using a Tecan Infinite 200 PRO spectrophotometer from China, with an excitation wavelength of 580 nm and an emission wavelength of 620 nm. The test was conducted independently on three separate occasions. The percentage change in F(AU) was determined by Eq. (2):

$$\mathrm{F(AU)} = \frac{\text{Sample treated with peptide} - \text{negative control}}{\text{Positive control} - \text{negative control}} \times 100. \tag{2}$$

LPS and PG Competitive Inhibition Assay

E. coli O111 B4 LPS (50 μL) and Nap* (50 μL, 4 × MIC) were combined in a 96-well plate and incubated at 37 °C for 1 h. Bacterial solutions containing 1×10^5 CFU/mL were then added to the LPS-derivative mixtures in 1.5 mL nonenzyme EP tubes and further incubated at 37 °C for 60 min. The concentration of LPS ranged from 2 to 1024 μg/mL, while the peptide concentration remained constant at 1 × MIC. After the incubation period, 50 μL of the mixture was transferred to MHA agar plates and cultured overnight. The following day, the number of colonies was counted. The trial was carried out three times, with two duplicates in every category. In the PG competition experiment, following an identical process, the final levels of POPC and POPG were 2–512 μg/mL.

Membrane Fluidity Assay

Following Kim's et al. [38] and Yang's et al. [39] report, a culture of *E. coli* ETEC K99 was grown overnight until it reached an OD_{600} of 0.4. Afterward, the culture was thinned to a density of 4×10^5 CFU/mL using HEPES buffer. Subsequently, it was mixed with Laurdan GP (2.5 mmol/L) and incubated in the dark at 37 °C for 60 min. Next, different amounts of Nap* (50 μL) were introduced and combined in a 96-well plate, and benzyl alcohol (3 mmol/L) served as the reference sample. The fluorescence intensities of Laurdan were determined by utilizing an F-4500 fluorescence spectrophotometer (manufactured by Hitachi, Japan) with an excitation wavelength of 492 nm and an emission wavelength of 435 nm. The temperature was kept constant at 37 °C during the measurement. The Laurdan generalized polarization (GP) was determined by utilizing Eq. (3):

$$\mathrm{GP} = \frac{(\mathrm{I435} - \mathrm{I490})}{(\mathrm{I435} + \mathrm{I490})}. \tag{3}$$

where I_{435} and I_{490} represent instantaneous fluorescence intensity at this wavelength, respectively.

Outer Membrane (OM) Permeabilization Assay

As described in Wang's et al. [17] report. In the OM permeabilization test, the N-phenyl-1-naphthylamine (NPN, Sigma−Aldrich) fluorescent probe was employed. *E. coli* ETEC K99, a Gram-negative bacterium, was chosen as the test sample. The background fluorescence was measured using an F-4500 fluorescence spectrophotometer (Hitachi, Japan) equipped with a 350-nm excitation wavelength and a 420-nm emission wavelength.

Respiratory Chain Dehydrogenase Viability Assay

The 2,3,5-triphenyltetrazolium chloride (TTC, Aladdin, 1 mg/mL) was used to evaluate the viability of *E. coli* ETEC K99 respiratory chain dehydrogenase. A solution containing Tris–HCl (50 mmol/L, pH 8.6), glucose (100 mmol/L), and TTC (1 mg/mL) was prepared, and 50 μL was placed in each well of a 96-well plate. Afterward, varying amounts of Nap* were introduced into every well, and then fresh bacterial solution ($OD_{600} = 0.2$) was added. The 96-well plate was incubated for 1.5 h at 37 °C, and the absorbance was assessed at 492 nm utilizing a microplate reader from Tecan GENios F129004, located in Austria.

CM Potential Assay

Changes in the electrical potential of the CM were observed by using the fluorescent dye $diSC_3$-5, which is responsive to membrane potential. *E. coli* ETEC K99 was grown until reaching the logarithmic growth phase, followed by dilution in HEPES buffer to reach an optical density of 0.05 at 600 nm. Under lightproof conditions, the resuspended cells were exposed to the $diSC_3$-5 probe for 60 min. Afterward, a mixture of peptide-$diSC_3$-5 (2 mL) was introduced into every well of a clean 24-well plate, and the fluorescence intensity was promptly assessed for 40 min (excitation λ = 620 nm, emission λ = 670 nm) after deducting the initial reading.

Inner Membrane (IM) Permeabilization Assay

To evaluate the permeability of the IM, we employed a synthetic o-nitrophenyl-β-D-galactopyranoside (ONPG) probe. *E. coli* ETEC K99 was cultured to the logarithmic growth phase in MHB medium supplemented with 2% lactose. The culture was then collected and diluted in PBS (10 mmol/L,

pH 7.4) to achieve an OD_{600} of 0.05. Next, the peptides were diluted using 50 μL of PBS, 50 μL of ONPG (6 mmol/L), and 100 μL of bacterial suspension. These mixtures were subsequently introduced into every well of the sterile 96-well plates. The absorbance was monitored by cyclical recording at OD_{420} for 100 min.

Fluorescence Microscopy Assay

To analyze the quality of membrane integrity, we used a fluorescence microscope (EVOS FL Auto, USA) in combination with a live/dead BacLight kit to evaluate the viability of bacterial. *E. coli* ETEC K99 in the mid-logarithmic growth phase was harvested through centrifugation at 5000 × *g* for 5 min and then diluted in PBS to obtain an optical density of 0.3 at OD_{600}. Various concentrations of Nap* were mixed with the bacteria for 1 h at 37 °C, and then the dyes were added and incubated for an extra 15 min. By utilizing the nucleic acid dyes SYTO 9 and PI, which possess varying capacities to infiltrate bacterial cells, a background of two-color fluorescence was attained.

Bacterial Agglutination Assay

The bacterial agglutination test involved culturing the *E. coli* cells until they reached the mid-log phase. Afterward, the specimens were spun at 3000 rpm for 5 min and then washed three times with HEPES buffer. To achieve an OD_{600} value of 0.3, the bacteria that were collected were suspended again in HEPES buffer. Various concentrations of the peptide were mixed with the bacterial solution in a cuvette sanitized with EtOH and incubated at room temperature for 8 h.

SEM and TEM Characterization

SEM and TEM were conducted after the peptides (1 × MIC) were incubated with *E. coli* cells. The cells were diluted to $OD_{600} = 0.3$ in 1 × PBS, and the plates were incubated at 37 °C for 60 min. The bacteria were collected and then treated with glutaraldehyde (2.5%, w/v) for 12 h to fix them. We observed morphological and ultrastructural alterations in the *E. coli* cells using a Hitachi Su-8010 SEM and a Hitachi H-7650 TEM, as detailed in our prior publications [40, 41].

Negative Staining TEM

E. coli ETEC K99 cells were mixed with Nap* nanofibers at a concentration of 8 μmol/L in HEPES buffer after being diluted to $OD_{600} = 0.2$ and incubated at 37 °C. Samples were gathered at various time points ($t = 0$, 2, 5, and 15 min) and thinned to a concentration lower than the MIC. Untreated *E. coli* cells served as controls at $t = 0$ min. Afterward, 10 μL of the diluted mixture was absorbed onto a carbon grid coated with 300-mesh copper for 2 min, and any extra solution was removed by blotting with filter paper. Following that, the cells were treated with 0.1% phosphotungstic acid for 10 s and dried naturally at room temperature for over 16 h. The Hitachi H-7650 transmission electron microscope (Hitachi, Japan) was used to analyze the structure of the *E. coli* microorganisms, with an acceleration voltage of 100 kV.

DNA Binding Assay

As described in Lai's et al. [40] report, total genomic DNA was extracted using a DNA isolation kit from Tiangen Biotech Co. Ltd., Beijing. In brief, the peptide samples were mixed with total genomic DNA extracted from *E. coli* ETEC K99 in a blend of binding buffer made up of 8 μL, 1 mmol/L EDTA, 10 mmol/L Tris–HCl (pH 8.0), 1 mmol/L dithiothreitol, 5% glycerol, 20 mmol/L KCl, and 50 mg/mL BSA. Afterward, the reaction mixtures were incubated at 37 °C for 1 h. Subsequently, native DNA loading buffer was introduced, and the samples underwent 1% agarose gel electrophoresis in 0.5 × TFE buffer.

ROS Generation Assay

E. coli cells were centrifuged at 5000 × g for 5 min and subsequently mixed with HEPES buffer at pH 7.4 until OD_{600} nm reached 0.4. Afterward, the bacterial solution was combined with varying amounts of Nap* and incubated for 50 min. Subsequently, a DCFH-DA probe (10 μmol/L) was introduced into the mixture of peptides and bacteria, followed by an hour of incubation. The intensity of fluorescence was evaluated by utilizing a 488 nm excitation wavelength and a 525 nm emission wavelength.

ATP Determination

Extracellular ATP concentrations of *E. coli* ETEC K99 were measured with an Enhanced ATP Assay Kit (Beyotime, catalog no. S0027). For the assay, mid-log-phase *E. coli* ETEC K99 cells were collected and thinned to $OD_{600} = 0.4$. Next, the bacterial cells underwent treatment with varying amounts of Nap* nanofibers, were then incubated for 60 min at 37 °C, and finally centrifuged at 12,000 rpm for 5 min at 4 °C. The bacterial precipitates were lysed using lysozyme (15 mg/mL), and the lysates were further centrifuged to obtain the intracellular ATP. The luminescence of the samples was measured using a spectrofluorophotometer (Tecan Infinite 200 Pro, China).

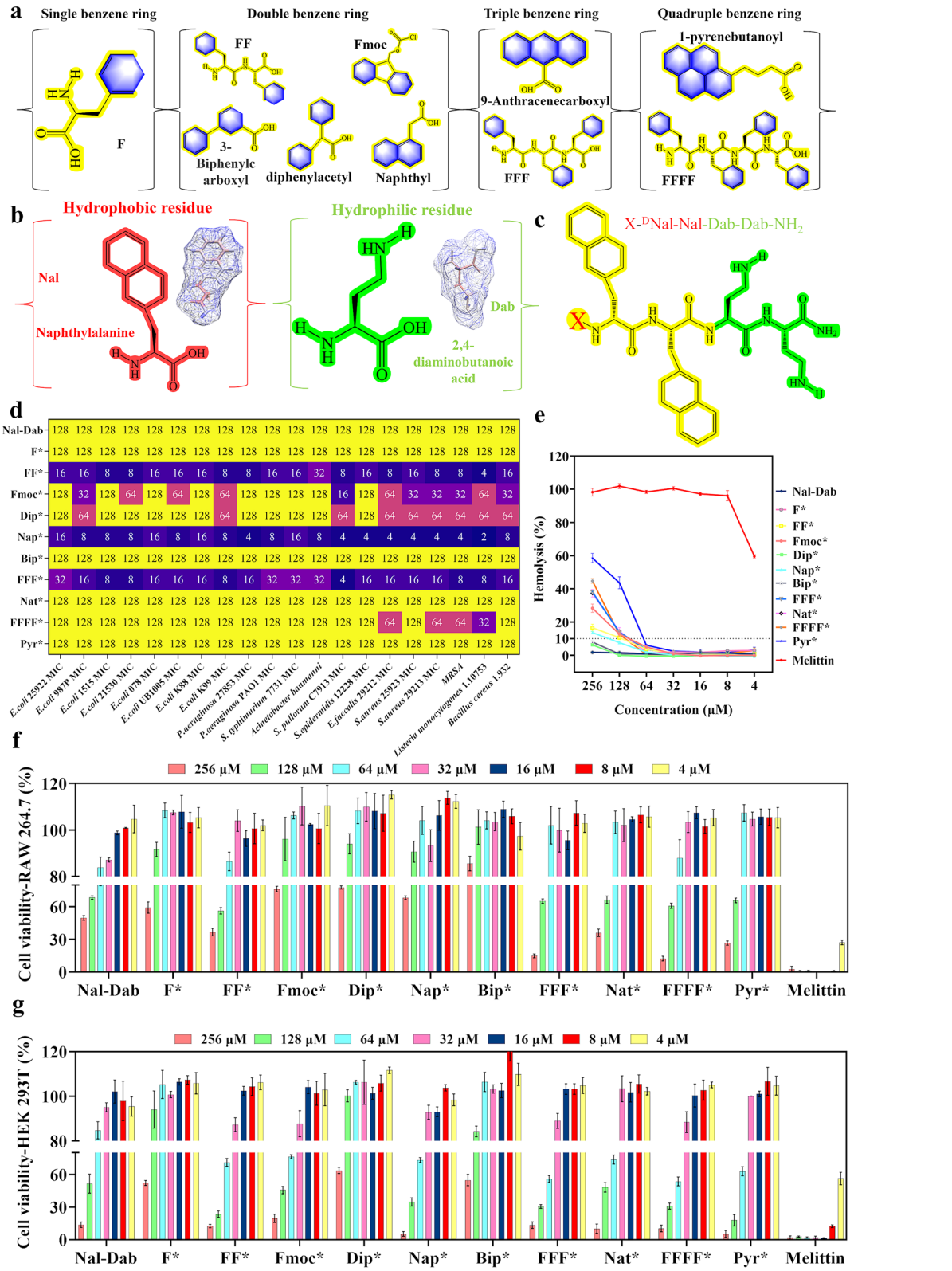

Fig. 1 The design principles of peptides, analysis of antimicrobial activity, and biocompatibility. **a** The chemical structure of the hydrophobic scaffold for attaching short peptide sequences. **b** Chemical structures of 1-naphthylalanine (Nal) and 2,4-diaminobutanoic acid (Dab). **c** Self-assembled antiproteolytic short peptide template. **d** MICs of self-assembled peptides. A value of 128 indicated the absence of detectable antimicrobial activity under the test conditions. **e** Hemolytic activity and cytotoxicity of self-assembling peptides to **f** RAW264.7 and **g** HEK 293 T cells

Intracellular pH Assay

E. coli ETEC K99 cells were washed, resuspended in HEPES buffer, and then diluted to $OD_{600} = 0.3$. Afterward, the medium was supplemented with the fluorescent dye BCECF-AM, reaching a concentration of 20 µmol/L. After the fluorescence was stabilized, various concentrations of Nap* were introduced. The 488 nm excitation wavelength and 522 nm emission wavelength were selected.

RNA Isolation and Transcriptome Analysis

The RNA was extracted and the transcriptome of *E. coli* ETEC K99 was analyzed by seeding the bacteria in MHB and allowing them to grow overnight at 37 °C. Next, the cells were thinned with new MHB and grown until they reached the middle logarithmic phase. Following three washes with HEPES, the *E. coli* cells were then centrifugation at $2000 \times g$ for 10 min and resuspended in HEPES buffer at a concentration of around 4×10^8 CFU/mL. After the cells were resuspended, they were incubated at 37 °C for 1 h in the presence of Nap* nanofibers (8 µmol/L) or HEPES. After incubation, total RNA was extracted from *E. coli* using the TRIzol technique following the manufacturer's instructions. Meige Gene Technology Co., Ltd. (Shenzhen, China) assessed the quality of the total RNA, then conducted RNA sequencing and data analysis. To eliminate ribosomal RNA, the Epicenter Ribo-Zero rRNA Removal Kit was used, while the NEB Next ® Ultra II ™ Directional RNA Library Prep Kit for Illumina was used to generate strand-specific libraries. Each group underwent three separate assays. The DESeq2 package was utilized for statistical analysis, with a corrected P value < 0.05 and $|\log_2(\text{fold-change})| > 1$ serving as the criteria for significant differential expression. To conduct enrichment analysis using GO and KEGG, a hypergeometric distribution was utilized along with a correction for the false discovery rate [42].

Non-targeted Metabolomic Analysis

Control group and Nap*-treated group samples were processed as described for the metabolomic analysis. 25 mg of sample was weighed and then 500 µL of extraction solvent, which consisted of a mixture of methanol, acetonitrile, and water in a ratio of 2:2:1 (v/v) with an isotopically labeled internal standard mixture, was added. The blend was evenly mixed at a frequency of 35 Hz for a duration of 4 min and then subjected to sonication for 5 min while placed in an ice-water bath. The steps were repeated a total of three times. The specimen was left at a temperature of − 40 °C for 1 h before being spun at 12,000 rpm at 4 °C for 15 min. The supernatant was transferred to an injection vial for analysis. The target compounds were chromatographically separated using a Vanquish ultrahigh-performance liquid chromatography system from Thermo Fisher Scientific equipped with a Waters ACQUITY UPLC BEH Amide column measuring 2.1 mm in diameter and 50 mm in length with a particle

Table 1 Therapeutic potential of the peptides

Peptide	GM_{MIC}[a]	HC_{10}[b]	IC_{20}[c]		SI[d]			GM_{SI}[e]
		hRBCs	RAW264.7	HEK293T	hRBCs	RAW264.7	HEK293T	
Nal–Dab	128	> 256	128	128	4	1	1	1.59
F*	128	> 256	256	256	4	2	2	2.52
FF*	11.71	128	128	64	10.93	10.93	5.47	8.68
Fmoc*	68.59	128	256	64	1.87	3.73	0.93	1.87
Dip*	93.70	> 256	256	256	5.46	2.73	2.73	3.44
Nap*	6.73	256	256	64	38.04	38.04	9.51	23.96
Bip*	128	> 256	> 256	256	4	4	2	3.17
FFF*	14.42	128	128	64	8.88	8.88	4.44	7.05
Nat*	128	128	128	64	1	1	0.5	0.79
FFFF*	107.63	128	128	64	1.19	1.19	0.59	0.94
Pyr*	128	128	128	64	1	1	0.5	0.79

[a]GM_{MIC}: geometric mean of the MIC values for the 20 bacteria tested

[b]HC_{10}: lowest peptide concentration that induces 10% hemolysis

[c]IC_{20}: minimum peptide concentration that causes 20% mammalian cell death

[d]SI: selectivity index = HC_{10} or IC_{20}/GM_{MIC}. When neither ≥ 10% hemolysis nor ≥ 20% cell death was detected at > 256 µmol/L, a concentration of 512 µmol/L was used to calculate the SI

[e]GM_{SI}: the geometric mean of the SI values of the engineered peptides against tested hRBCs, RAW 264.7 cells, and HEK 293 T cells was calculated

size of 1.7 μm. The Orbitrap Exploris 120 mass spectrometer acquired first- and second-level mass spectrometry data under the control of Xcalibur software (version: 4.4, Thermo). The original data were transformed into mzXML format through the use of ProteoWizard software, followed by peak identification, extraction, alignment, and integration using a custom R package that utilizes XCMS as its central component. Data analysis was performed by Meige Gene Technology Co., Ltd. (Shenzhen, China).

In Vivo Toxicity Assay

24 female ICR mice, all healthy and weighing 20.26 ± 2.49 g, were acquired from Liaoning Changsheng Biotechnology Company in Benxi, China. The mice, aged 6–8 weeks, were divided into four cages, each containing 6 mice. The mice were given standard commercial diets and deionized water at the correct temperature, then given 3 days to adjust. Control group mice were given intraperitoneal saline, whereas the remaining three groups were injected with Nap* nanofibers intraperitoneally at 5, 10, and 20 mg/kg doses for three days in a row. Body weight changes were monitored during the entire experiment. On the fourth day, mild ether anesthesia was administered for euthanasia. Blood samples were collected from the orbital veins of the mice for the evaluation of serum biochemical levels. The liver, spleen, and kidney were extracted and measured to calculate their respective organ weights in relation to body weight. Tissue samples for morphological studies were fixed in 4% paraformaldehyde and then underwent H&E staining. Equation (4) for calculating the organ index was as follows:

$$\text{Organ index}\,(\%) = \frac{\text{Organ weight}\,(g)}{\text{Mouse weight}\,(g)} \times 100. \tag{4}$$

In Vivo Peritonitis–Sepsis Model

The procedures for raising mice and collecting organs were carried out using identical protocols to those used for the in vivo toxicity experiments. Twenty-four female ICR mice, between 6 and 8 weeks old and weighing 20.31 ± 1.26 g, were divided into three groups randomly, each containing 8 mice. The groups received a 100 μL intraperitoneal injection of an *E. coli* ETEC K99 suspension in saline, containing an $OD_{600} = 0.3$. This concentration effectively ensured the survival of mice. Subsequently, the mice that were challenged received treatment with either saline (100 μL), Nap* (10 mg/kg), or gentamicin (3 mg/kg) via intraperitoneal injection at 0.5 h and 2 h after infection. The three animal groups were euthanized after 8 h. Blood samples were collected to assess the serum cytokine levels. The liver, kidney, and spleen were divided into sections for H&E staining, with the rest of the organs being weighed, rinsed in saline, and homogenized promptly with a homogenizer [43]. Subsequently, the homogenized mixture was diluted as needed, plated on prepared MHA, and incubated overnight at 37 °C, with the count of colonies per gram of tissue being calculated.

Checkerboard Assay

The combined impact of Nap* and antibiotics was evaluated through checkerboard assays based on established procedures [18, 44]. A 96-well plate was prepared with BSA solution (50 μL) in each well. Nap* and antibiotics were diluted along the vertical and horizontal axes, respectively. Subsequently, 50 μL of *E. coli* cells at a final concentration of 1×10^5 CFU/mL was introduced into every well. FIC values were calculated by assessing the absorbance at 492 nm after 18–24 h of incubation at 37 °C. The FIC index was then calculated using Eq. (5):

$$\text{FIC} = \frac{\text{MIC Nap} * \text{ in combination}}{\text{MIC Nap} *} + \frac{\text{MIC antibiotic in combination}}{\text{MIC antibiotic}}. \tag{5}$$

The resulting FIC indices were used to classify the interactions as synergistic (FIC index ≤ 0.5), additive (0.5 < FIC index < 1), no interaction (1 ≤ FIC index ≤ 4), or antagonistic (FIC index > 4) effects.

Anti-biofilm Activity Assays

The ability of Nap* to inhibit biofilm formation was evaluated in 96-well plates (Corning Inc., NY) through a crystal violet staining assay. To summarize, cultures of *P. aeruginosa* ATCC 27853 were grown in TSB medium until they reached the mid-logarithmic phase and then diluted 100 times with fresh TSB medium. Afterward, 100 μL of the diluted bacterial mixture and different amounts of Nap* were introduced into individual wells of a 96-well plate. To allow biofilm development, the plate was incubated at 37 °C for 24 h. Following the removal of the TSB medium, the wells were washed with PBS to remove any free-floating bacteria. Afterward, the adherent biofilms were stained with a 0.1% (w/v) solution of crystal violet (100 μL) for 10 min at ambient temperature and then washed with PBS to eliminate any excess dye. To dissolve the dye, 200 μL of a 70% ethanol solution was added to each well following the drying process. The biofilm biomass was determined by measuring the absorbance at 595 nm using a microplate reader (Tecan GENios F129004, Austria) for three separate experiments performed in triplicate.

Disruption of Preformed Biofilms

To disrupt biofilms that had already formed, cultures of *P. aeruginosa* ATCC 27853 in the mid-log phase were diluted by a factor of 100 in TSB medium. Then, 100 µL of this diluted culture was added to each well. Afterward, the plates were placed in an incubator at 37 °C for 24 h to promote biofilm development. Following biofilm formation, PBS was used to wash each well, and then 100 µL of Nap* at different concentrations was added. After exposure to Nap* for 4 h, the wells were once again rinsed with PBS. Biofilm viability was then assessed then conducted using the crystal violet staining assay following the aforementioned procedure. Every trial was performed in triplicate and replicated independently on three occasions.

Ethics Statement

Northeast Agricultural University's Institutional Animal Care and Use Committee approved the procedures for this research. The care and handling of animals followed the guidelines outlined in the 2016 revision of the "Regulations for the Management of Laboratory Animals" in Heilongjiang Province, China.

Statistical Analysis

Quantitative data are presented as the mean ± standard deviation (SD) and were analyzed using GraphPad software (GraphPad Prism 9, for Windows). Statistical significance was determined using one-way ANOVA with Duncan's multiple range test. Statistical significance is denoted as $*P < 0.05$, $**P < 0.01$, $***P < 0.001$, and $****P < 0.0001$ (comparing the mean of each group with the mean of a control group). A P value less than 0.05 was considered to indicate statistical significance. Significant differences between groups are indicated by different lowercase letters (a, b, and c) for P values < 0.05 and (A, B, and C) for P values < 0.01 (comparing the mean of each group with the mean of every group).

Results and Discussion

Engineered Peptide Library Screening and Bioactivity Analysis

Generally, achieving enhanced antimicrobial activity relies on an amphiphilic substance that enables the disruption of bacterial membranes [45]. The inclusion of hydrophilic cationic charges and hydrophobic residues in the amphiphilic structure initiates electrostatic interactions with negatively charged bacterial membranes [8, 29], facilitating the penetration of antibacterial agents into the lipophilic domain of the bacterial membrane. Therefore, to incorporate hydrophobic groups, a series of polycyclic compounds were employed to construct nanoscaffolds, including single (phenylalanine, F), double (FF, Fmoc, 3-biphenylcarboxyl, diphenylacetyl and naphthyl), triple (FFF, 9-anthracenecarboxyl) and quadruple (FFFF, 1-pyrenebutanoyl) benzene rings (Fig. 1a). Our strategies are as follows: (i) we explored the potential relationships between various benzene ring numbers and short peptide sequences in terms of antibacterial activity, cytotoxicity, and self-assembly properties. (ii) Due to their considerably larger cross-sectional areas compared to those of linear alkyl chains, which are conducive to self-assembly, we subjectively excluded aliphatic hydrophobic stents. (iii) They are resistant to hydrolysis by proteases. Among the hydrophobic amino acids, Phe is considered to increase the affinity of peptides for membrane interfaces and thus further enhance their assembly capacity [46]. Therefore, the mutant of Phe (Nal) was chosen to increase the resistance to enzymolysis (Fig. 1b). Among the hydrophilic amino acids, the mutant of lysine (Dab) conferred a positive charge on the peptide sequence, and the mutant of arginine (Arg) was not chosen because the guanidine side chain might cause unnecessary loss of biocompatibility. In addition, Arg residues are known to be more readily recognized by trypsin, which would compromise the peptide stability [17, 20]. The presence of long side chains in the amino acid mutants of Arg might inadvertently result in undesirably decreased resistance to enzymatic hydrolysis. The final self-assembled short peptide template was X–^{D}Nal–Nal–Dab–Dab–NH_2, where X represents the nanoscaffold (Fig. 1c). A surfactant structure model was used for the template, and the benzene ring side chains of the first chiral Nal and the second Nal were situated in the same plane to increase the intermolecular π–π stacking interactions, facilitating self-assembly of the peptide [47]. The charge and stability of the peptide were both further achieved by amidation of the C-terminus. Characterization was performed using reverse-phase high-performance liquid chromatography (RP-HPLC) and matrix-assisted laser desorption/ionization time-of-flight mass spectrometry (MALDI-TOF–MS) during the synthesis process. The measured relative molecular masses of the peptides closely matched their theoretical values, indicating successful synthesis. Furthermore, the peptides exhibited purity of more than 95%, thus validating their exceptional quality (Figs. S1 and S2). The first three letters of the nanoscaffolds were used to name the corresponding peptides. The chemical structures of all the engineered peptides are presented in Fig. S3.

The critical aggregation concentration (CAC) determines the self-assembly characteristics of engineered peptides. Hence, the self-assembly capability and CAC of the engineered peptides were examined using 1-anilino-8-naphthalene sulfonate (ANS) fluorescence for analysis in aqueous medium [12]. As shown in Figs. S4 and S5, with increasing

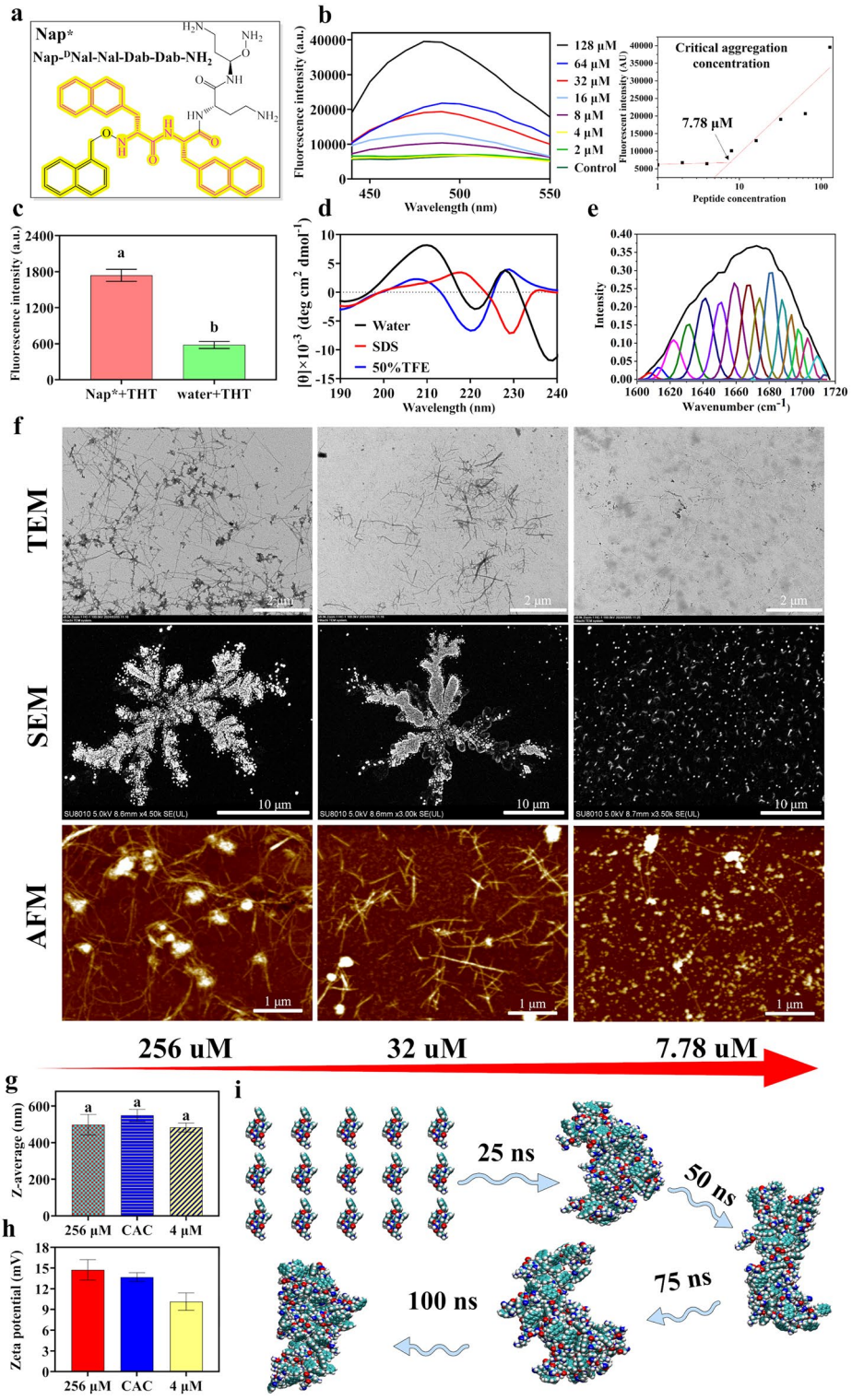

Fig. 2 Fabrication and characterization of Nap* nanofibers. **a** The chemical structure of Nap*. **b** Concentration-dependent self-assembly of Nap* in aqueous solution and its CAC. **c** ThT fluorescence analysis of Nap*. The values represent the mean ± standard deviation, with a sample size of $n = 6$. Groups distinguished by distinct superscripted letters (a, b) indicate a significant difference ($P < 0.05$). **d** CD spectra of Nap* (64 μmol/L) in aqueous solution or SDS (30 mmol/L) and 50% TFE. **e** Fitting of the amide I band in the FTIR spectrum of Nap* using OMNIC 8.2 software. **f** TEM, SEM and AFM images of Nap* at concentrations of 256, 32 and 7.78 μmol/L in aqueous solution. **g** The size distribution of Nap* was measured by dynamic light scattering, and **h** the zeta potential. **i** Molecular dynamics simulation images of Nap* within 100 ns

concentration, the amphiphilic molecules with double, triple and quadruple benzene rings showed a significantly increased in ANS fluorescence intensity, indicating that the multiring hydrophobic groups play a crucial role in driving the formation of self-assembled structures in short peptides. However, the initial short peptide sequence (Nal–Dab), the single benzene ring peptide (F*) and the double benzene ring peptide (Dip*) did not exhibit a significant redshift in ANS fluorescence intensity. These findings suggested that the hydrophobicity of a single Phe residue alone was not sufficient to drive the formation of self-assembled structures by the short peptide sequence. Moreover, the excessive rigidity of the diphenylacetyl group might affect the transformation of the peptide chain into an ordered secondary structure, leading to the disruption of self-assembled structures [47]. Next, the antimicrobial effectiveness of the engineered peptides was assessed using MIC and MBC assays (Figs. 1d and S6), which included studies in Gram-negative and Gram-positive bacteria, respectively. To assess the antimicrobial activity of the peptides more intuitively, the geometric mean (GM) was used to calculate the MIC of the peptides. The initial short peptide sequence (Nal–Dab) and F* did not exhibit any antimicrobial activity (MIC > 128 μmol/L). However, F*, FF*, FFF*, and FFFF* exhibited a trend toward increased antibacterial activity, which then decrease with an increase in the number of hydrophobic amino acid repeats in the engineered peptides, suggesting that a specific number of hydrophobic amino acid residues is necessary for the peptide activity. A crucial threshold for the hydrophobicity of the peptides also exists, above which the efficacy of the peptides ceases to increase, or the peptides can even lose their biological activity [18]. Among the nanoscaffold peptides composed of polycyclic compounds, bicyclic compounds exhibited better antibacterial activity, while tricyclic and tetracyclic compounds did not show significant antibacterial effects under the test conditions, which further confirmed the threshold number of hydrophobic groups. However, engineered peptides with bicyclic structures showed significantly different antibacterial activities, indicating that spatial positioning is an important factor influencing the antibacterial activity of the peptides, even when the number of benzene rings is the same [12, 48]. Among them, Nap* exhibited the greatest biological activity against both Gram-negative and Gram-positive bacteria (GM_{MIC} = 6.73) (Table 1).

Another challenge for the systematic management of AMP biomaterials is their potential cytotoxicity to mammalian cells; consequently, the hemolytic activity and cytotoxicity of the engineered peptide were assessed for compatibility with various cell types, including human embryonic kidney (HEK 293 T) cells, mouse macrophage (RAW 264.7) cells, and human red blood cells (hRBCs). As shown in Fig. 1e–g all engineered peptides exhibited negligible cytotoxicity at concentrations below 64 μmol/L. However, when the concentration exceeded 64 μmol/L, the hemolytic activity and cytotoxicity of the engineered peptides increased in a dose-dependent manner, with stronger toxicity observed as the number of benzene rings increased. Strong hydrophobic interactions might directly regulate the depth of amphiphilic molecule insertion into the eukaryotic lipid membrane and thus the ability to induce lysis of the eukaryotic cell membrane [29]. To identify the most promising engineered peptides, the baseline for hemolysis was set at 10% hRBC, and the baseline for mammalian cell toxicity was set at 80% cell viability. The results indicated that naphthyl might be the most suitable for incorporation into short peptide sequences, as it exhibited the optimal balance of between peptide self-assembly, cytotoxicity, and antimicrobial activity in our tests. Because Nap*(GM_{SI} = 23.96), FF* (GM_{SI} = 8.68) and FFF* (GM_{SI} = 7.05) were in subordinate positions (Table 1). Due to the optimal engineered peptide Nap* exhibited the highest geometric mean selectivity index, Nap* was selected for the investigation of a series of subsequent indicators.

Characterization of the Self-Assembling Short Peptide Nap*

Theoretically, Nap* should penetrate into the cell interior by means of a surfactant structure, effectively incorporating hydrophobic residues and causing the formation of micellar structures by exposing water molecules. However, the naphthyl, ^{D}Nal, and Nal residues contribute to the lateral extension of micellar molecules along the main axis through stable π–π stacking. The stable aggregation ability of the molecular framework (Fig. 2a) was potentially facilitated by the cation–π interactions and hydrophobic aggregation resulting from the interaction between Dab and the aromatic system, as well as the cross-interaction induced by the structure of the surfactant. This combination enabled the self-assembly process to drive the formation of amyloid-like fiber structures in their lowest energy conformation. The ANS assay revealed a rapid increase in the fluorescence intensity of Nap* with increasing concentration (Fig. 2b). The fluorescence intensity values of ANS at 485 nm for different peptide concentrations were fitted with two straight lines, indicating that Nap* started to form oligomers at a concentration of 7.78 μmol/L. Thioflavin T (ThT) fluorescence analysis initially confirmed the presence of amyloid-like fiber structures in Nap* (Fig. 2c). The dye specifically interacted with the amyloid-like protein structures, inducing changes in their spectral characteristics that serve as indicators of the presence of amyloid-like protein conformations [49]. ThT molecules are speculated to align parallel to the original fiber axis when interacting with the fiber molecules, and upon binding with Nap*, the fluorescence intensity exhibited a redshift due to an expanded π-conjugation resulting from interaction with the *β*-sheet structure [50]. Therefore, to reveal

the potential self-assembly mechanism of Nap*, we further investigated the conformational trends of Nap* in various simulated environments to provide further insights into the secondary structures supporting amyloid-like fibers. Ordered secondary structures have been acknowledged in numerous studies as a prerequisite for nanostructure formation [8, 11, 12, 51]. Therefore, circular dichroism (CD) was employed to investigate the secondary conformations of Nap* in various settings (Fig. 2d). In the water and 50% TFE (hydrophobic environment) environment, Nap* showed negative peaks near 205–210 nm and positive peaks at ≈ 220 nm, indicating that Nap* was primarily characterized by a β-sheet tendency. A faint β-turn signal was also observed, manifested as a positive peak at approximately 230 nm. In SDS (a simulated negatively charged membrane), the faint signal of β-turns disappeared, possibly due to the integration of β-strands into more advanced structures [8]. However, CD only exhibited spectral data primarily dominated by β-sheets, and Fourier transform infrared spectroscopy (FTIR) was further analyzed to explore all the secondary structural parameters of Nap* (Fig. 2e). The results indicated that the anti-parallel β-sheets peak at approximately 1670 cm^{-1}–1690 cm^{-1} dominated at a percentage of 31.6%. α-Helix signals were also observed at 1650 cm^{-1}–1660 cm^{-1} (26.3%), suggesting that Dab induced partial helical structures. The next structural categories are parallel β-sheets (14.5%), β-turns (14%) and random coils (13.6%). This indicated that Nap* first forms distinct secondary structures in aqueous solution and then collaboratively drives the formation of higher-level self-assemblies.

Next, the Nap* nanomorphology in aqueous solution was directly observed via transmission electron microscopy (TEM), scanning electron microscopy (SEM), and atomic force microscopy (AFM) (Fig. 2f). First, Nap* (2.56 mmol/L) was subjected to overnight aging and diluted to 7.78 μmol/L (CAC), 32 μmol/L and 256 μmol/L, after which it was allowed to rest for 24 h. At 7.78 μmol/L of Nap*, TEM revealed only short and thin nanofibers. In addition, small amounts of spherical micelles were observed by SEM and AFM, indicating that in the early stage of Nap* self-assembly, β-sheet and α-helical structures promoted the formation of nanofibers and spherical micelles, respectively. As the concentration increased to 32 μmol/L and 256 μmol/L, Nap* further self-assembled into supramolecular nanostructures. Antiparallel β-sheets predominated and drove Nap* to form twisted and compact fibrous structures, indicating the concentration-driven self-assembly of Nap*. The distribution of nanoparticles in solution was measured by dynamic light scattering (DLS), which revealed their evenness (Fig. 2g), including the water layer surrounding the nanoparticles within the calculation range [52]. With increasing concentration (4, CAC, 256 μmol/L), the dynamic diameter of the spherical micelles formed by Nap* did not significantly increase remained approximately 500 nm. This further indicates that the spherical micelles were not the primary self-assembled entities, and nanofibers were the main mode of Nap*. The zeta potential findings indicated that Nap* nanofibers possess multiple positive surface charges, which are necessary for AMPs to achieve systemic effectiveness by maintaining electrostatic attraction to anionic microbial membranes (Fig. 2h).

Finally, molecular simulation programs were used to describe the details of the internal molecular motion of Nap* in aqueous solution at the microscale (Fig. 2i). According to the results of the GROMACS simulations, the root mean square deviation (RMSD) was used to represent the consistency of the structures before and after the simulation (Fig. S7). The conformational perturbation of the assembly occurred only at ≈ 1000 ps and stabilized at ≈ 10,000 ps, indicating that Nap* reached the desired stability rapidly. The number of intermolecular hydrogen bonds showed a stable increasing trend during the testing time (Fig. S8). The gyration radius (Rg) and solvent-accessible surface area (SASA) were used to evaluate the compactness of the peptide structure (Figs. S9 and S10). A decrease in their number signifies an increase in intermolecular cohesion between peptides, suggesting molecular aggregation.

In Vitro Barrier Penetration of Nap* Nanofibers Under Physiological Conditions

As the main goal of this study, we initially assessed the protease resistance of Nap* nanofibers. To align with the in vivo application of antimicrobial agents, we selected trypsin, chymotrypsin, and pepsin as the test proteases. Trypsin is reported to cleave preferentially at the C-terminus of arginine and lysine, chymotrypsin prefers to cleave at the C-terminus of phenylalanine and tryptophan, and pepsin exhibits specific cleavage activity toward aromatic amino acids [13, 17, 20]. Thus, FF* and FFF* were chosen as controls since they are theoretically sensitive to chymotrypsin and pepsin. We incubated the tested peptide (1.28 mmol/L) with protease (at final concentrations of 10, 5, 2.5 and 1.25 mg/mL) for 1 h, and the antibacterial activity of the Nap* nanofibers against *E. coli* ETEC K99 remained essentially unchanged (Fig. 3a). In the presence of moderate to high concentrations of chymotrypsin (≥ 2.5 mg/mL), FF* exhibited a partial loss of antimicrobial activity, while FFF* exhibited complete loss of its antimicrobial activity (Fig. S11). This may indicate that the efficiency of aromatic amino acid cleavage by proteases depends on the quantity of aromatic amino acids present. However, FF* and FFF* were able to resist the effects of low to moderate concentrations (chymotrypsin ≤ 1.25 mg/mL, pepsin ≤ 2.5 mg/mL). This may be attributed to the self-assembled system that partially shields the cleavage sites of the proteases, thereby retaining partial antimicrobial activity of the peptides [12, 13, 49, 53, 54]. Nap* nanofibers combined the advantages of enzymatic resistance sequences

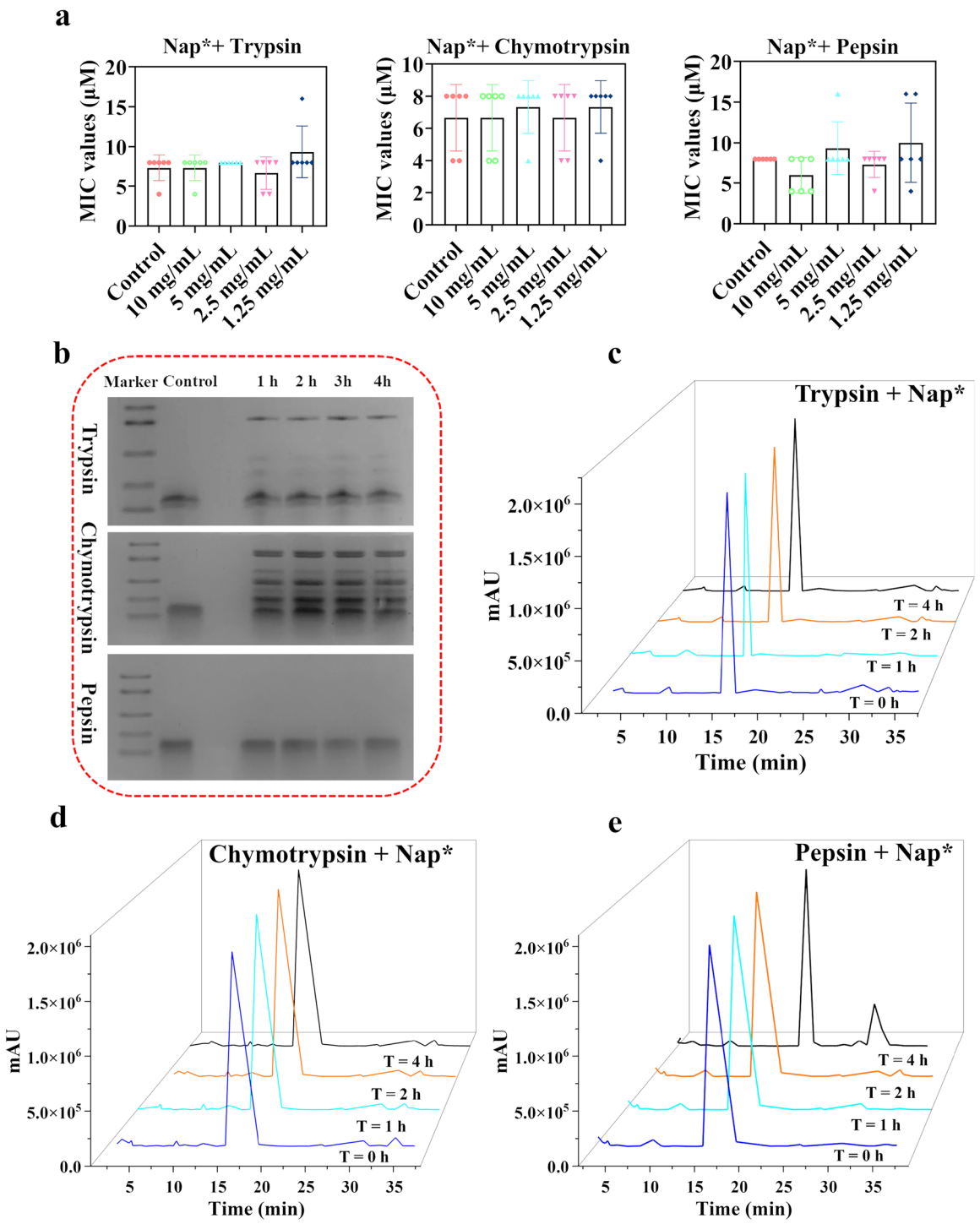

Fig. 3 Analysis of the enzyme resistance of Nap* nanofibers in vitro. **a** MIC of Nap* against *E. coli* ETEC K99 after incubation for 1 h with different concentrations of trypsin, chymotrypsin and pepsin. The control group results were obtained from the MIC assay. The values are presented as the mean ± standard deviation (SD), $n = 6$. **b** Cleavage of Nap* by trypsin, chymotrypsin and pepsin. The peptides were incubated with 10 mg/mL protease for 1, 2, 3 and 4 h at 37 °C, and the molecular weights of the protein markers from top to bottom were 31, 20.1, 14.4, 6.5 and 3.3 kDa. **c** RP-HPLC analysis of the Nap* nanofibers after incubation with 10 mg/mL trypsin, **d** chymotrypsin, or **e** pepsin for 0, 1, 2 and 4 h

with a self-assembled system, achieving complete resistance against the tested proteases. Even under the condition of coexistence of three enzymes, the antimicrobial efficacy of Nap* was minimally affected, as evidenced by variations in MIC values of only up to twofold after incubation for 48 h at the highest combined enzyme concentration (10 mg/mL) (Fig. S12). Subsequently, the retention of Nap* nanofibers after protease treatment was determined using 16.5% tricine–SDS–polyacrylamide gel electrophoresis (PAGE). The concentrations of proteases used were very close to the levels found in simulated intestinal and gastric fluids (10 mg/mL) [19, 29]. Figure 3b shows that Nap* nanofibers exhibited protein bands similar to those of the control after incubation with 10 mg/mL protease for 1–4 h. Similarly, the RP-HPLC profile showed that Nap* nanofibers exhibited high retention under trypsin and chymotrypsin treatment, with a single peak area accounting for more than 85% (Fig. 3c, d). However, after 4 h of treatment with pepsin, additional peaks appeared, indicating slight cleavage of Nap* (Fig. 3e). The analysis of the bactericidal kinetics of Nap* against *E. coli* ETEC K99 revealed the elimination of all bacteria within 15 min at a concentration of 1 × MBC, which was significantly faster than the rate of Nap* nanofiber cleavage by pepsin, indicating that it may possess clinical potential (Fig. S13).

Different concentrations of physiological salts and serum were utilized to assess the suitability of the Nap* nanofibers (Fig. S14). Among the seven physiological salts examined, only Ca^{2+} had a significant impact on Nap*, increasing its MIC against *E. coli* ETEC K99 by fourfold. This may be attributed to the competitive binding of Ca^{2+} to lipopolysaccharides (LPS) on the microbial membrane surface, which increases membrane rigidity and ultimately decreases the antibacterial efficacy [55]. Subsequently, we examined the stability of the Nap* nanofibers after exposure to 100%, 50% and 25% human serum. Even after incubation in 100% pure human serum for 4 h, the Nap* nanofibers retained significant antibacterial activity, indicating that the enzymes present in the serum were insufficient to degrade Nap*.

In summary, the Nap* nanofibers exhibited high stability against proteases, physiological salt ions, and serum. Advances in the combination of short peptide protease-resistant sequences with self-assembly systems would boost the therapeutic capacity of these systems and expedite their clinical translation.

Proposed Overall Antimicrobial Mechanisms of Nap* Nanofibers

Based on the substantial surface charge of the nanofibers, it was proposed that Nap* exhibits similar membrane action to AMPs. To examine the logical consistency and credibility of the mechanism, a comprehensive membrane operation system was devised by integrating nanofibers. Different manipulations of *E. coli* ETEC K99 membranes have been described, encompassing external to internal aspects, quantitative to qualitative analyses, and investigations of features from molecular components to morphology. FITC-labeled Nap* nanofibers and propidium iodide (PI) were employed to initially examine the location of action of Nap* nanofibers via confocal laser scanning microscopy (CLSM). The results showed that Nap* nanofibers labeled with FITC were decentralized on the *E. coli* ETEC K99 surface (Fig. 4a).

To confirm whether the initial binding sites of the Nap* nanofibers were located on the outer membrane surface, LPS was initially chosen for examination. LPS binding ratios exceeding 80% at elevated nanofiber concentrations (≥ 16 μmol/L) indicated that Nap* was oriented on the Gram-negative membrane occurred via electrostatic attraction. With decreasing Nap* concentration and probe displacement, noticeable or progressive transmutation was observed (Fig. 4b). To evaluate the impact of LPS on antimicrobial efficacy, a combination of LPS and Nap* was incubated for 1 h, followed by the introduction of *E. coli* ETEC K99. The bactericidal effects of the Nap* nanofibers were completely hindered when the concentration of dissociated LPS reached 512 μg/mL, providing further evidence that Nap* initially attaches to LPS (Fig. S15). Phosphatidylglycerol (PG) is another crucial component of bacterial cell membranes and plays a vital role in stabilizing the bacterial membrane [56]. In the presence of free PG, the antimicrobial activity of Nap* decreased, suggesting that PG may serve as another binding site or target for Nap* (Fig. S16). In contrast, neutral phosphatidylcholine (PC) did not exhibit a similar effect. The combination of nanofibers with negatively charged LPS and PG is likely to disrupt the fluidity and permeability of lipid bilayers or alter the lipid packing density [57, 58]. The fluorescence intensity was significantly higher in the presence of Laurdan GP, a dye sensitive to membrane fluidity, indicating that Nap* reduced membrane fluidity in *E. coli* ETEC K99 (Fig. 4c). This decrease in fluidity could contribute to passive membrane permeabilization, structural destabilization, and dysregulated ion medium activity [38, 59].

Subsequently, we investigated the disruptive impacts of nanofibers on bilayer lipid membranes by perturbing membrane fluidity. Compared with Gram-positive bacteria, Gram-negative bacteria possess an outer membrane (OM) that provides superior protection [60, 61]. The fluorescence intensity of the N-phenyl-1-naphthylamine (NPN) probe increased in a dose-dependent manner with the concentration of Nap*, indicating the formation of fiber aggregates on the OM surface. At a concentration of 16 μmol/L, the permeability of the OM reached over 90% (Fig. 4d). The observed reduction in the activity of respiratory chain dehydrogenases provides further evidence of membrane

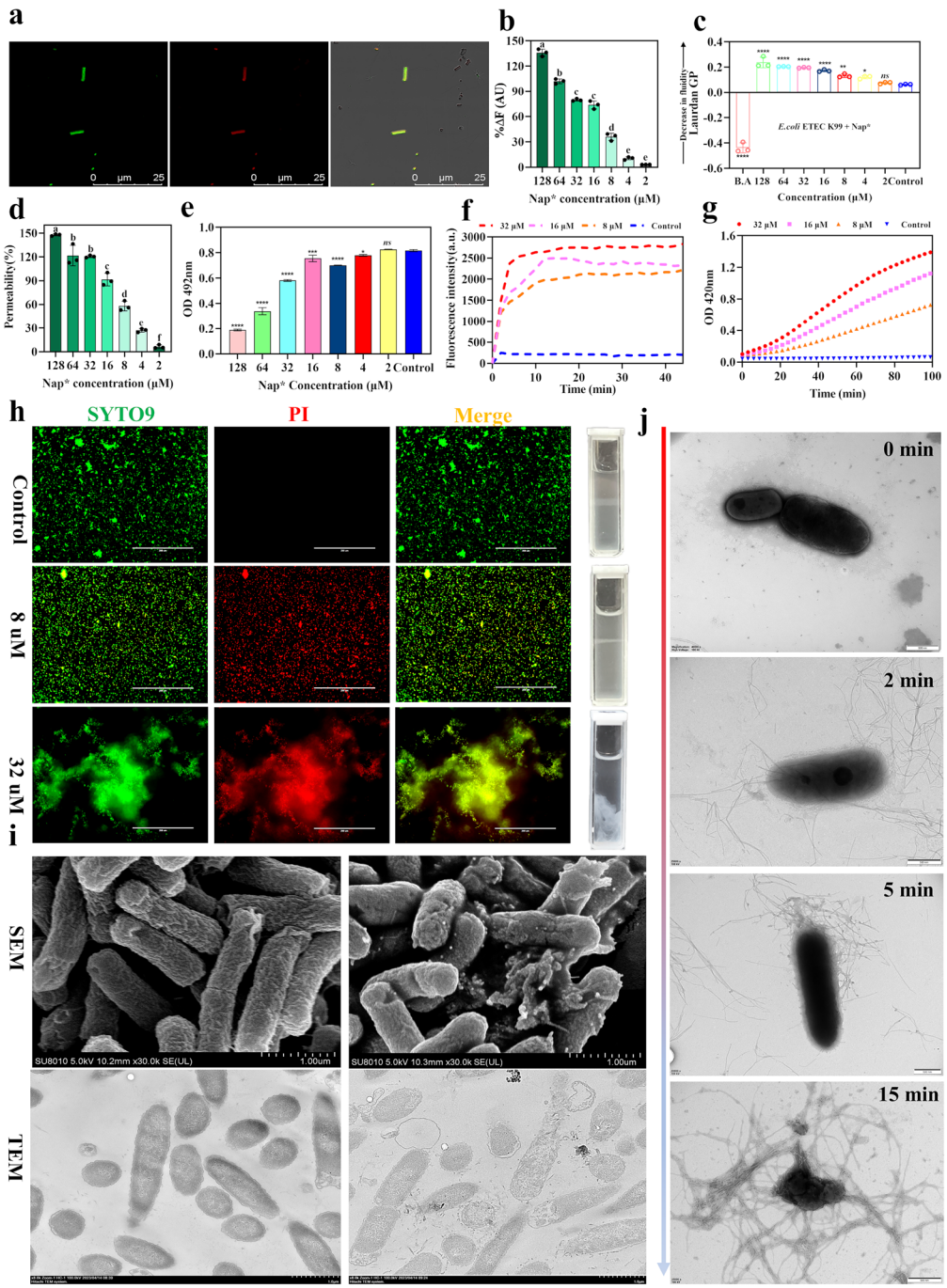

Fig. 4 Nap* nanofibers induce bacterial death through membrane disruption. **a** CLSM observations. Green signal: FITC-label, red signal: PI. **b** The LPS binding affinities of Nap*. The data are presented as the mean ± standard deviation (SD), $n = 3$. Differences among groups exposed to different concentrations of Nap* were assessed using one-way ANOVA, followed by Tukey's post hoc analysis; (a, b…) indicate a significant difference ($P < 0.05$). **c** Effect of Nap* on the membrane fluidity of *E. coli* ETEC K99. The data points were collected from three biologically independent experiments. The error bars indicate the mean ± SD. Statistical analysis was performed using one-way ANOVA followed by multiple comparisons to determine the significance of differences between the control and Nap* treatment groups (*$P < 0.05$, **$P < 0.01$, ***$P < 0.001$, ****$P < 0.0001$). **d** Outer membrane permeability induced by Nap*. **e** The inhibitory effect of Nap* on the activity of respiratory chain dehydrogenases in *E. coli* cells. **f** Cytoplasmic membrane depolarization induced by the Nap* nanofibers. **g** Inner membrane permeability induced by Nap* nanofibers. **h** Live/dead fluorescence image and bacterial agglutination assay of *E. coli* ETEC K99 treated with Nap*. Scale bar: 200 μm. **i** SEM and TEM images of *E. coli* ETEC K99 after treatment with Nap* nanofibers at 37 °C for 1 h. The control (left) was incubated at 37 °C for 1 h without the addition of Nap*. **j** Negative-stained TEM images of *E. coli* ETEC K99 after exposure to Nap* nanofibers for varying durations are presented. Images at time points ranging from 0 to 15 min were obtained

disruption. As the respiratory chain of *E. coli* ETEC K99 is located on the plasma membrane [62], the direct targeting of the plasma membrane by Nap* inhibits respiratory chain dehydrogenase activity (Fig. 4e). Due to the aggregation of these nanofibers, the cytoplasmic membrane potential is vulnerable to instability. Next, the Nap* nanofibers permeated the inner membrane (IM) layer, resulting in significant and rapid depolarization of the cytoplasmic membrane in *E. coli* ETEC K99 cells. This depolarization was contingent on both time and dose, leading to uncontrolled ion flux, loss of membrane potential, and eventual impairment of the IM (Fig. 4f, g) [63, 64].

To explore the mechanistic correlation in more detail, we employed a series of microscopic imaging techniques to investigate the deeper alterations in the internal and external morphology of *E. coli* cells following treatment with Nap*. The LIVE/DEAD assay showed that upon the addition of SYTO 9, the nanofiber-induced membrane damage led to a gradual merging of SYTO 9's staining with the red signal of PI. The simultaneous presence of the two stains led to the emergence of a chartreuse color (Fig. 4h). In addition, when the concentration of Nap* reached 32 μmol/L, the *E. coli* cells underwent bacterial aggregation, indicating the possible activation of an alternative antibacterial mechanism, in which the entrapment and killing of bacteria by a high concentration of nanofiber network prevented their escape [10, 19, 49, 65]. The bacterial aggregation test conducted in an EtOH-sterilized cuvette corroborated this observation, as *E. coli* cells treated with 32 μmol/L Nap* displayed visible bacterial clustering, while the groups treated without Nap* or with 8 μmol/L Nap* did not exhibit this phenomenon. In the TEM micrographs, the bacterial membranes and cytoplasm of all the *E. coli* ETEC K99 cells were distinctly visible, and the SEM micrographs revealed the smooth surface of the cells. Upon treatment with Nap*, the TEM images revealed cytoplasmic content leakage, the formation of blebs, vacuolization, and the presence of broken *E. coli* cells. Similarly, SEM revealed crumpled cells and fragments. These observations unequivocally confirmed that the Nap* nanofibers induced membrane disruption (Fig. 4i). The negative staining TEM images of *E. coli* following treatment with Nap* nanofibers at various time intervals provided a comprehensive understanding of the temporal dynamics and underlying mechanisms of action (Fig. 4j). During 2-min and 5-min incubation periods, we observed the adhesion of Nap* nanofibers to the surface of the *E. coli* cells, with a significant number of Nap* nanofibers successfully penetrating the OM and entering the cell interior. Ultimately, at 15 min, significant cytoplasmic shrinkage and disrupted *E. coli* cells were evident.

The membrane damage enables us to intrude into the cell to investigate signals associated with cell death. Once nanofibers enter the interior of *E. coli* cells, they first bind to DNA (Fig. S17), preventing its migration; subsequently, Nap* triggers oxidative stress and inflicts damage upon the bacteria by disrupting their respiratory processes, leading to the overproduction of reactive oxygen species (ROS) (Fig. S18) and ultimately increasing the internal pH of *E. coli* cells (Fig. S19), inducing ATP leakage (Fig. S20). In previous studies, AMPs and bio-nanomaterials have been found to potentially disrupt genetic-level interactions, thereby affecting biological processes [29, 66–69]. To further elucidate the intracellular disruptive effect of Nap* nanofibers, we performed transcriptomic and metabolomic analyses on *E. coli* ETEC K99 treated with Nap*(1 × MIC). The results indicated that *E. coli* cells exhibited 276 significantly differentially expressed genes (a total of 3875 genes identified) following treatment with Nap* nanofibers (P values < 0.05, FDR ≤ 0.05 and fold-change (FC) ≥ 2) (Figs. 5a and S21). Among these genes, 161 genes were upregulated, and 115 genes were downregulated (Fig. S22). Moreover, Gene Ontology (GO) and Kyoto Encyclopedia of Genes and Genomes (KEGG) enrichment analyses (Fig. S23) confirmed that the differentially expressed genes affected by Nap* nanofibers were most enriched in the plasma membrane and involved in interfering with the expression of membrane protein and inner membrane protein genes (ybjM, ybhL, yohK, yohj, nlpA, ydjZ, yidD, ybaN, yhiD, yjiG), and the genes encoding ABC transporters and proteins associated with transmembrane transport were significantly inhibited, which confirmed that Nap* directly targets mechanisms associated with the *E. coli* cell membrane (Fig. S24). In addition to the confirmed the disruption of the cytoplasmic membrane, Nap*-induced differential gene expression was found to originate from pathways related to sulfur metabolism, nitrogen metabolism, nucleotide metabolism, biotin metabolism, amino acid metabolism, carbohydrate metabolism, and energy metabolism (Figs. S25 and S26). Nap* significantly downregulated the pyruvate dehydrogenase gene and the E2 subunit (aceF), thereby attenuating the irreversible oxidative decarboxylation of pyruvate to acetyl-CoA. Consequently, an increase in the expression levels of succinate dehydrogenase complex flavoprotein subunits (sdhD, sdhA, and sdhC) forced the bacteria to perform glycolysis and oxidative phosphorylation to compensate for the loss of the tricarboxylic acid (TCA) cycle (Fig. S27), which is consistent with our previous finding that Nap* induces ATP leakage. Furthermore, numerous genes involved in DNA replication and transcription exhibited differential expression in *E. coli* following Nap* treatment (Figs. S25 and S26). These genes are associated with transcription factors as well as purine, pyrimidine, and amino acid metabolism, indicating that Nap* also interferes with transcription and translation functions. In the nontargeted metabolomics analysis, 71 differentially abundant metabolites were enriched (Fig. 5b), revealing changes in intracellular amino acids,

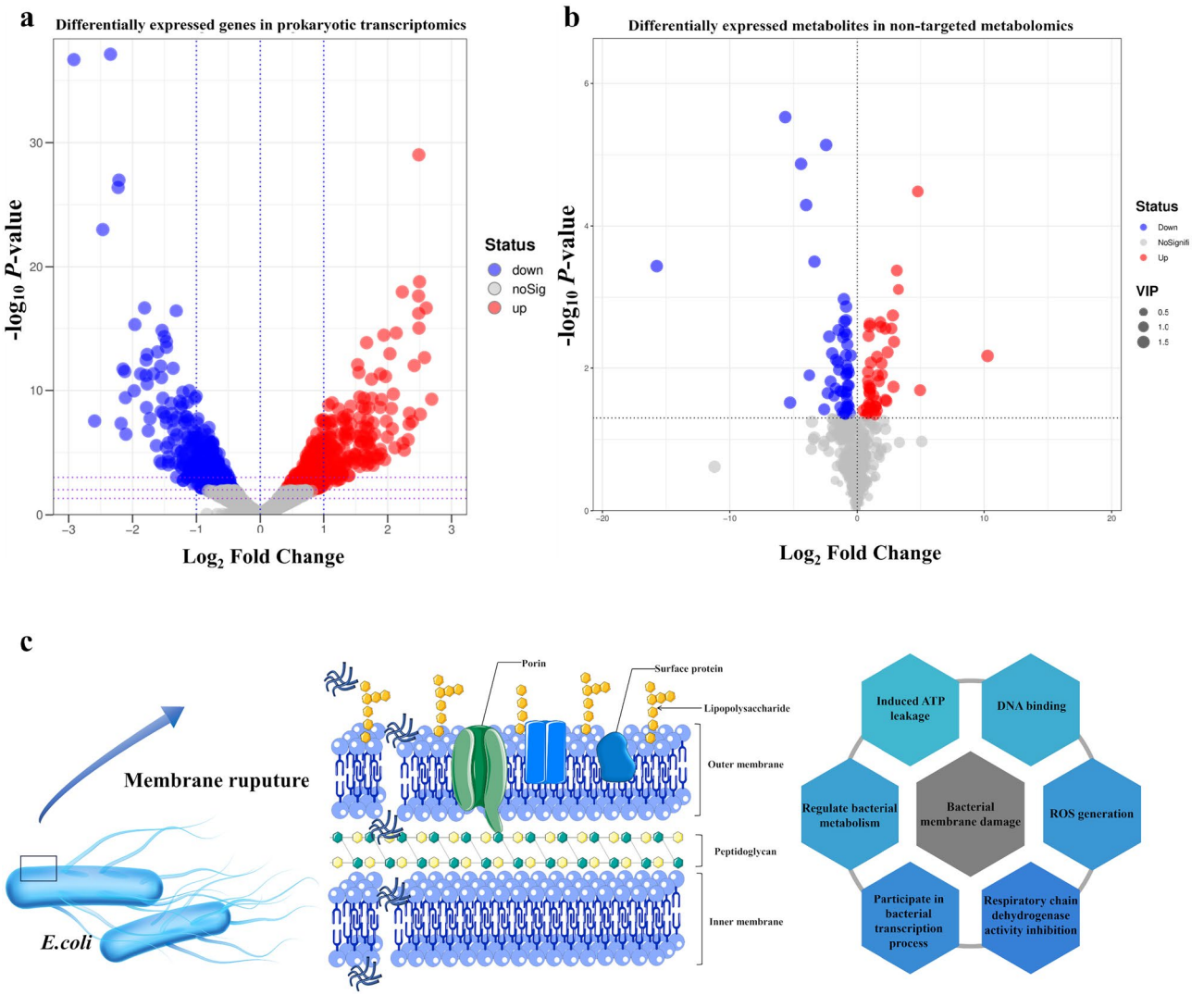

Fig. 5 Whole-transcriptome RNA sequencing and nontargeted metabolome sequencing revealed that Nap* nanofibers disrupted normal bacterial cellular activities. **a** Volcano plots of differentially expressed genes between *E. coli* cells treated with Nap* and control cells. The blue dots and rose-red dots represent downregulated and upregulated differentially expressed genes, respectively; the white dots represent genes without significantly differential expression. The horizontal axis represents the log 2 of the fold-change values, while the vertical axis represents the negative log 10 of the *P* values. **b** Volcano plots of differentially expressed metabolites. **c** Schematic diagram illustrating the multimodal synergistic mechanism of *E. coli* cell death induced by Nap*

glycerol phospholipids, nucleosides, and organic acids in *E. coli* following Nap* treatment (Figs. S28–S32). The downregulation of amino acid and nucleoside metabolites confirmed the findings from the transcriptomic investigation.

In summary, Nap* targets the LPS and PG on the bacterial membrane, electrostatically adsorbs to the OM surface and further disrupts the OM, causing strong fluctuations in the membrane potential of *E. coli* cells and inducing IM damage. At high concentrations, the nanofiber network captures bacteria, preventing their escape. When Nap* enters the intracellular environment, it first binds to negatively charged DNA, then induces the accumulation of ROS and triggers ATP leakage and pH elevation. At the genetic level, Nap* can elicit comprehensive responses in processes such as transcription, translation, energy production, and transmembrane transport. These findings suggested that Nap* promotes apoptosis in *E. coli* cells through multiple synergistic modes of action (Fig. 5c).

Evaluation of In Vivo Biocompatibility and Treatment of Systemic Bacterial Infection

The successful in vitro efficacy of the Nap* nanofibers prompted us to transition to in vivo investigations to explore their therapeutic potential in peritonitic–septicemic mice infected with *E. coli* ETEC K99. Prior to that, Nap*

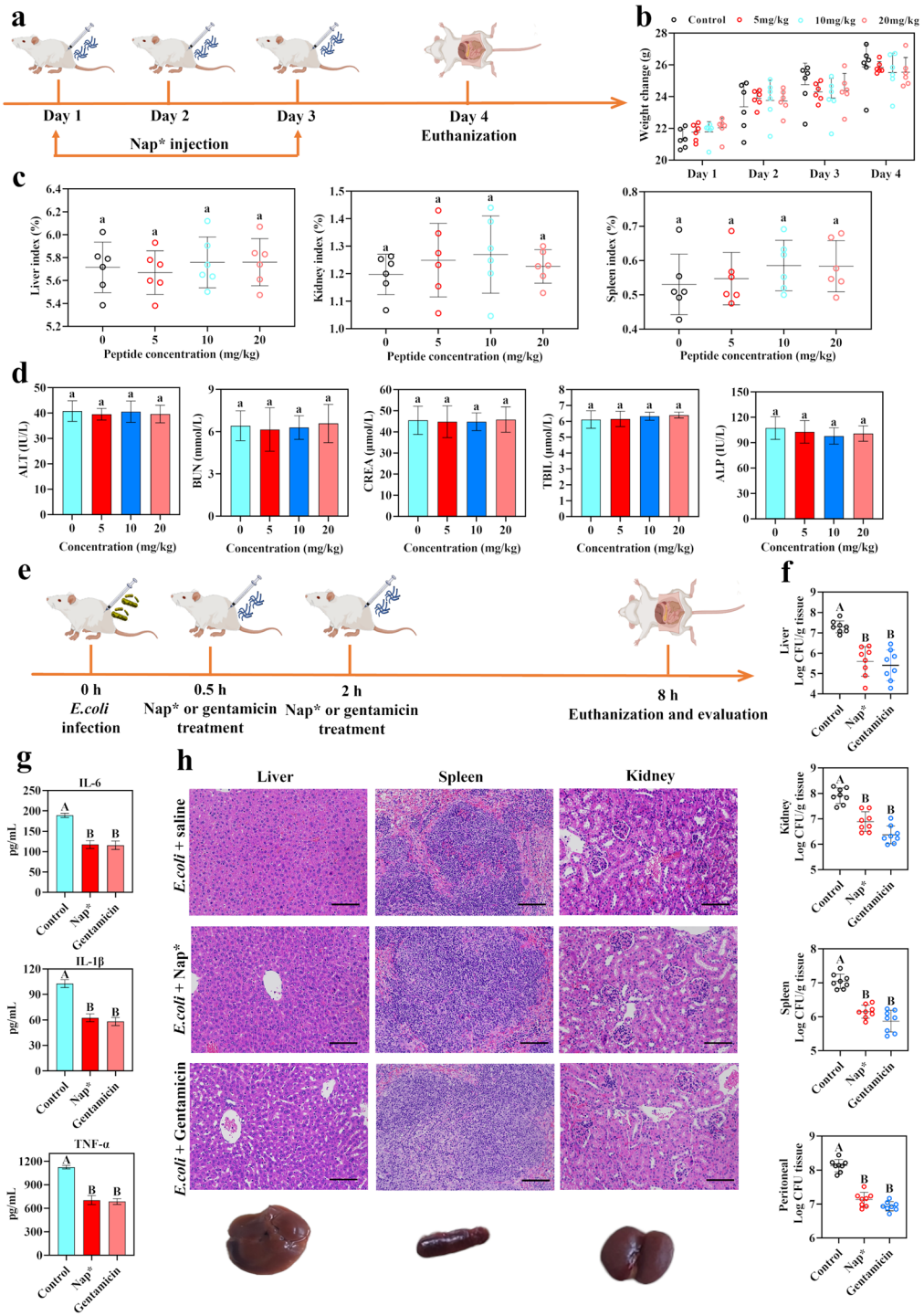

Fig. 6 Nap* nanofibers exhibit excellent in vivo biocompatibility and therapeutic potential in peritonitis–sepsis models. **a** Schematic illustration of the in vivo biocompatibility measurement protocol. **b** Changes in the weight curve and **c** relative organ index (mean ± SD, $n = 6$, $P > 0.05$). **d** Liver, kidney, and spleen function parameters of mice injected with 5, 10, or 20 mg/kg of the substance and saline for 4 days were assessed and expressed as the mean ± SD ($n = 6$). There were no statistically significant differences between the groups ($P > 0.05$). **e** Schematic illustration of the experimental protocol for measuring efficacy. **f** Bacterial load of *E. coli* cells in the liver, kidney, spleen and peritoneum after infection with *E. coli* cells and treatment with saline, Nap* nanofibers and gentamicin. A and B indicate significant differences ($P < 0.01$). **g** Effects on the IL-6, IL-1β, and TNF-α levels in mouse serum. The data are shown as the mean ± SD ($n = 8$). **h** Histopathological H&E staining of the liver, kidney and spleen. Significant differences between groups are denoted by distinct lowercase letters (a, b, and c) for P values < 0.05 and uppercase letters (A, B, and C) for P values < 0.01

nanofibers were administered via intraperitoneal injection to ICR female mice to assess their in vivo safety (Fig. 6a). Following the injection, the mice were carefully observed for indications of pain and any alterations in weight. Two mice that received injections of 20 mg/kg Nap* displayed different levels of hind limb movement sluggishness, listlessness, and decreased mobility within 1 h, suggesting that systemic stimulation of the mice by Nap* at a high dose (20 mg/kg) was transient, with only a brief duration (Fig. S33). Furthermore, following three days of uninterrupted administration of Nap*, the body weight of the mice exhibited a consistent upward trend (Fig. 6b), with no notable significant differences in the organ (liver, kidney or spleen) index or weight changes between the control group (saline) and the injected group ($P > 0.05$) (Fig. 6c). Subsequently, blood biochemical markers reflecting the health status of the spleen, kidney, and liver were analyzed to assess in vivo biocompatibility. The levels of blood urea nitrogen (BUN), creatinine (CREA), alanine aminotransferase (ALT), alkaline phosphatase (ALP), and total bilirubin (TBIL) in the serum exhibited no significant differences ($P > 0.05$), indicating that the administration of Nap* did not induce hepatotoxicity or nephrotoxicity (Fig. 6d). In contrast to those in the control group (saline), the liver, kidney, and spleen tissues treated with 5, 10, and 20 mg/kg Nap* nanofibers exhibited no pathological alterations. The tissues displayed clear visibility of the hepatic portal vein and hepatic stroma, intact renal tubules and collecting ducts, and distinct splenic sinus tissue, indicating the marked biocompatibility of Nap* nanofibers (Fig. S34).

Given the inconsequential in vivo toxicity of Nap* nanofibers, their potential biomedical application was further evaluated by assessing their effectiveness in a mouse model of peritonitic–septicemic infection. As shown in Fig. 6e, at 0 h, *E. coli* ETEC K99 at an infectious dose ($OD_{600} = 0.35$, 100 μL was injected into the abdominal cavity of each mouse, and at 0.5 h and 2 h, the mice were administered different treatments (control group: *E. coli* + saline; Nap* group: *E. coli* + 10 mg/kg; gentamicin group: 3 mg/kg). After a period of 8 h, the mice were euthanized, and their livers, kidneys and spleens were extracted, homogenized, diluted, and subjected to culture. The plate culture results demonstrated a notable reduction in the bacterial load within the liver, kidney, spleen and peritoneum of the treated mice, but no significant difference was observed compared with that in the group treated with gentamicin ($P > 0.01$) (Fig. 6f).

Nap* may exhibit dual properties, initially capturing bacteria within the peritoneal cavity to prevent their extensive spread and invasion. Subsequently, Nap* directly kills the escaped *E. coli* cells located on the surfaces of organs or within tissues. The levels of proinflammatory cytokines (including IL-6, IL-1β, and TNF-α) in the serum were significantly lower in the Nap* nanofiber-treated group than in the group treated with saline (Fig. 6g). According to the histological analysis results, mice treated with saline exhibited extensive tissue damage, including symptoms of hepatic cell congestion, inflammatory cell infiltration, proliferation of splenic sinus connective tissue, abnormal morphology of the renal tubules and collecting ducts, and atrophy of the renal glomeruli. In contrast, Nap* nanofiber treatment alleviated this tissue damage (Fig. 6h). Therefore, the findings from the peritonitic–septicemic infection model underscore the potential of Nap* nanofibers as a treatment option for bacterial infections in vivo.

Future Research on Nap* Nanofibers

In previous studies, peptides have been used in combination with antibiotics to reduce the dosage of antibiotics and prevent the emergence of multidrug-resistant bacteria [18, 63, 70]. Therefore, we tested the combination of Nap* nanofibers with clinically available antibiotics against Gram-negative bacteria. The results indicated that Nap* nanofibers exhibited an additive effect when combined with peptide-based antibiotics, penicillins, certain aminoglycosides, and macrolides (Table S1). However, no interactions were observed with cephalosporins, tetracyclines, or quinolones. Therefore, future research will focus on exploring the bactericidal mechanisms and in vivo application potential of Nap* nanofibers in combination with commercially available antibiotics. The aim is to reduce the antibiotic dosage and align it with clinical usage. Furthermore, we discovered that Nap* could inhibit and eradicate the biofilm produced by *P. aeruginosa* ATCC 27853 (Fig. S35). This has sparked interest in exploring the ability of Nap* to inhibit higher-level bacterial community effects. Future challenges will focus on addressing treatment dilemmas in community hospitals and animal husbandry.

Conclusions

In summary, we identified the versatile Nap* nanofibers in a screen of self-assembled systems based on different numbers of benzene rings combined with enzyme-resistant sequences composed of nonnatural amino acids. We systematically investigated the nanoscale characteristics, in vitro and in vivo antimicrobial activities, biocompatibility, and bactericidal mechanisms of Nap*. Furthermore, the Nap* nanofibers showed strong tolerance to physiological conditions and protease invasion, demonstrating their potential application in treating systemic infections. The mechanistic results indicated that Nap* nanofibers can capture and aggregate bacteria, preventing their dispersion and evasion. Moreover, membrane disruption, ATP leakage and ROS accumulation were all extensively induced inside *E. coli* cells. These processes also interfere with transcription, translation, and energy metabolism, exhibiting a multimodal synergistic

mechanism to drive cell death. In conclusion, the combination of self-assembled systems with short peptide sequences provides a novel approach that could offer a theoretical basis for peptide-based nanomaterials and present promising candidate materials for addressing clinical challenges.

Supplementary Information The online version contains supplementary material available at https://doi.org/10.1007/s42765-024-00410-y.

Acknowledgements This work was supported by the National Natural Science Foundation of China (Nos. 32030101, 32272914, and 32002215), the Heilongjiang Provincial Collaborative Innovation Achievement Project for Universities—Incubation Project (LJGXCG2022-022), the Heilongjiang Touyan Innovation Team Program (No.54600112) and the Natural Science Foundation of Heilongjiang Province (YQ2022C015). The authors thank Baojing Cheng and Zhongyu Li for their assistance in providing the experimental instruments and thank Yinfeng Lv and Zhanyi Yang for their valuable guidance on this article.

Authors Contributions W.K.Y. and A.S.S. formulated and planned the experimental design. W.K.Y., X.G., Q.R.L., X.F.L., Y.X.W., C.X.S., and L.C.Z. performed the primary experimental assays. W.K.Y. authored the main manuscript. J.J.W. and A.S.S. provided oversight and supervision throughout the work and revised the final version of the manuscript. All authors have thoroughly reviewed and approved the final version of the manuscript.

Funding National Natural Science Foundation of China, 32030101, Anshan Shan, 32272914, Anshan Shan, 32002215, Jiajun Wang, Heilongjiang Provincial Collaborative Innovation Achievement Project for Universities—Incubation Project, LJGXCG2022-022, Anshan Shan, Heilongjiang Touyan Innovation Team Program, 54600112, Anshan Shan, Natural Science Foundation of Heilongjiang Province, YQ2022C015, Changxuan Shao.

Data availability Data are available upon reasonable request.

Declarations

Conflict of interest The authors declare no conflict of interest.

References

1. Tacconelli E, Carrara E, Savoldi A, Harbarth S, Mendelson M, Monnet DL, Pulcini C, Kahlmeter G, Kluytmans J, Carmeli Y, Ouellette M, Outterson K, Patel J, Cavaleri M, Cox EM, Houchens CR, Grayson ML, Hansen P, Singh N, Theuretzbacher U, Magrini N. Discovery, research, and development of new antibiotics: the WHO priority list of antibiotic-resistant bacteria and tuberculosis. *Lancet Infect Dis*. **2018**;*18*:318–27.
2. Magana M, Pushpanathan M, Santos AL, Leanse L, Fernandez M, Ioannidis A, Giulianotti MA, Apidianakis Y, Bradfute S, Ferguson AL, Cherkasov A, Seleem MN, Pinilla C, de la Fuente-Nunez C, Lazaridis T, Dai T, Houghten RA, Hancock REW, Tegos GP. The value of antimicrobial peptides in the age of resistance. *Lancet Infect Dis*. **2020**;*20*:e216–30.
3. Gao N, Wang JJ, Fang CY, Bai PF, Sun Y, Wu WP, Shan AS. Combating bacterial infections with host defense peptides: shifting focus from bacteria to host immunity. *Drug Resist Updat*. **2024**;*72*:101030.
4. Li WL, Xiao XM, Qi YC, Lin XH, Hu HQ, Shi MQ, Jiang WA, Liu LQ, Chen K, Wang K, Liu RH, Zhou M. Host-defense-peptide-mimicking β-peptide polymer acting as a dual-modal antibacterial agent by interfering quorum sensing and killing individual bacteria simultaneously. *Research*. **2023**;*6*:0051.
5. Shan JY, Che JY, Song CH, Zhao YJ. Emerging antibacterial nanozymes for wound healing. *Smart Med*. **2023**. https://doi.org/10.1002/SMMD.20220025.
6. Abadehie FS, Dehkordi AH, Zafari M, Bagheri M, Yousefiasl S, Pourmotabed S, Mahmoodnia L, Validi M, Ashrafizadeh M, Zare EN, Rabiee N, Makvandi P, Sharifi E. Lawsone-encapsulated chitosan/polyethylene oxide nanofibrous mat as a potential antibacterial biobased wound dressing. *Eng Regen*. **2021**. https://doi.org/10.1016/j.engreg.2022.01.001.
7. Fang YX, Zhu YH, Li L, Lai ZH, Dong N, Shan AS. Biomaterial-interrelated bacterial sweeper: simplified self-assembled octapeptides with double-layered trp zipper induces membrane destabilization and bacterial apoptosis-like death. *Small Methods*. **2021**;*5*:e2101304.
8. Wang CS, Shao CX, Fang YX, Wang JJ, Dong N, Shan AS. Binding loop of sunflower trypsin inhibitor 1 serves as a design motif for proteolysis-resistant antimicrobial peptides. *Acta Biomater*. **2021**;*124*:254–69.
9. Lande R, Gregorio J, Facchinetti V, Chatterjee B, Wang YH, Homey B, Cao W, Wang YH, Su B, Nestle FO, Zal T, Mellman I, Schröder JM, Liu YJ, Gilliet M. Plasmacytoid dendritic cells sense self-DNA coupled with antimicrobial peptide. *Nature*. **2007**;*449*:564–9.
10. Chu H, Pazgier M, Jung G, Nuccio SP, Castillo PA, de Jong MF, Winter MG, Winter SE, Wehkamp J, Shen B, Salzman NH, Underwood MA, Tsolis RM, Young GM, Lu W, Lehrer RI, Bäumler AJ, Bevins CL. Human α-defensin 6 promotes mucosal innate immunity through self-assembled peptide nanonets. *Science*. **2012**;*337*:477–81.
11. Yu WK, Wang JJ, Wang ZH, Li LX, Li WY, Song J, Zhang SS, Shan AS. PEGylation of the antimicrobial peptide PG-1: a link between propensity for nanostructuring and capacity of the antitrypsin hydrolytic ability. *J Med Chem*. **2021**;*64*:10469–81.
12. Yu WK, Sun Y, Li WY, Guo X, Liu XS, Wu WP, Yu WQ, Wang JJ, Shan AS. Self-assembly of antimicrobial peptide-based micelles breaks the limitation of trypsin. *ACS Appl Mater Interfaces*. **2023**;*15*:494–510.
13. Lai ZH, Yuan XJ, Chen HY, Zhu YH, Dong N, Shan AS. Strategies employed in the design of antimicrobial peptides with enhanced proteolytic stability. *Biotechnol Adv*. **2022**;*59*:107962.
14. Li GY, Lai ZH, Shan AS. Advances of antimicrobial peptide-based biomaterials for the treatment of bacterial infections. *Adv Sci*. **2023**;*10*:e2206602.
15. Di YP, Lin Q, Chen C, Montelaro RC, Doi Y, Deslouches B. Enhanced therapeutic index of an antimicrobial peptide in mice by increasing safety and activity against multidrug-resistant bacteria. *Sci Adv*. **2020**;*6*:eaay6817.
16. Pan M, Lu C, Zheng MC, Zhou W, Song FL, Chen WD, Yao F, Liu DJ, Cai JF. Unnatural amino-acid-based star-shaped poly(L-Ornithine)s as emerging long-term and biofilm-disrupting antimicrobial peptides to treat pseudomonas aeruginosa-infected burn wounds. *Adv Healthc Mater*. **2020**;*9*:e2000647.
17. Wang JJ, Song J, Yang ZY, He SQ, Yang Y, Feng XJ, Dou XJ, Shan AS. Antimicrobial peptides with high proteolytic resistance for combating gram-negative bacteria. *J Med Chem*. **2019**;*62*:2286–304.
18. He SQ, Yang ZY, Li XF, Wu H, Zhang LC, Shan AS, Wang JJ. Boosting stability and therapeutic potential of proteolysis-resistant antimicrobial peptides by end-tagging β-naphthylalanine. *Acta Biomater*. **2023**;*164*:175–94.

19. He SQ, Yang ZY, Li XF, Zhang LC, Wang JJ, Shan AS. Optimized proteolytic resistance motif (DabW)-based U1-2WD: a membrane-induced self-aggregating peptide to trigger bacterial agglutination and death. *Acta Biomater*. **2022**;*153*:540–56.
20. Zhu YJ, Shao CX, Li GY, Lai ZH, Tan P, Jian Q, Cheng BJ, Shan AS. Rational avoidance of protease cleavage sites and symmetrical end-tagging significantly enhances the stability and therapeutic potential of antimicrobial peptides. *J Med Chem*. **2020**;*63*:9421–35.
21. Shao CX, Jian Q, Li BW, Zhu YJ, Yu WK, Li ZY, Shan AS. Ultrashort all-hydrocarbon stapled α-helix amphiphile as a potent and stable antimicrobial compound. *J Med Chem*. **2023**;*66*:11414–27.
22. Cai XM, Dong J, Liu J, Zheng HZ, Kaweeteerawat C, Wang FJ, Ji ZX, Li RB. Multi-hierarchical profiling the structure-activity relationships of engineered nanomaterials at nano-bio interfaces. *Nat Commun*. **2018**;*9*:4416.
23. Cruz MA, Bohinc D, Andraska EA, Alvikas J, Raghunathan S, Masters NA, van Kleef ND, Bane KL, Hart K, Medrow K, Sun M, Liu H, Haldeman S, Banerjee A, Lessieur EM, Hageman K, Gandhi A, de la Fuente M, Nieman MT, Kern TS, Maas C, de Maat S, Neeves KB, Neal MD, Gupta AS, Stavrou EX. Nanomedicine platform for targeting activated neutrophils and neutrophil-platelet complexes using an α(1)-antitrypsin-derived peptide motif. *Nat Nanotechnol*. **2022**;*17*:1004–14.
24. Herrera-Barrera M, Ryals RC, Gautam M, Jozic A, Landry M, Korzun T, Gupta M, Acosta C, Stoddard J, Reynaga R, Tschetter W, Jacomino N, Taratula O, Sun C, Lauer AK, Neuringer M, Sahay G. Peptide-guided lipid nanoparticles deliver mRNA to the neural retina of rodents and nonhuman primates. *Sci Adv*. **2023**;*9*:eadd4623.
25. An HW, Mamuti M, Wang XF, Yao HD, Wang MD, Zhao LN, Li LL. Rationally designed modular drug delivery platform based on intracellular peptide self-assembly. *Exploration*. **2021**. https://doi.org/10.1002/exp.20210153.
26. Feng XF, Hou XL, Cui CJ, Sun SB, Sadik S, Wu SH, Zhou F. Mechanical and antibacterial properties of tannic acid-encapsulated carboxymethyl chitosan/polyvinyl alcohol hydrogels. *Eng Regen*. **2021**. https://doi.org/10.1016/j.engreg.2021.05.002.
27. Chen Y, Yuan ZC, Sun WY, Shafiq M, Zhu J, Chen JF, Tang H, Hu L, Lin WK, Zeng YX, Wang L, Zhang L, She YL, Zheng H, Zhao GF, Xie D, Mo XM, Chen C. Vascular endothelial growth factor-recruiting nanofiber bandages promote multifunctional skin regeneration via improved angiogenesis and immunomodulation. *Adv Fiber Mater*. **2023**;*5*:327–48.
28. Wang ZJ, Hu WK, Wang W, Xiao Y, Chen Y, Wang XH. Antibacterial electrospun nanofibrous materials for wound healing. *Adv Fiber Mater*. **2023**;*5*:107–29.
29. Lai ZH, Jian Q, Li GY, Shao CX, Zhu YJ, Yuan XJ, Chen HY, Shan AS. Self-assembling peptide dendron nanoparticles with high stability and a multimodal antimicrobial mechanism of action. *ACS Nano*. **2021**;*15*:15824–40.
30. Li P, Zhou C, Rayatpisheh S, Ye K, Poon YF, Hammond PT, Duan HW, Chan-Park MB. Cationic peptidopolysaccharides show excellent broad-spectrum antimicrobial activities and high selectivity. *Adv Mater*. **2012**;*24*:4130–7.
31. Wang C, Hong TT, Cui PF, Wang JH, Xia J. Antimicrobial peptides towards clinical application: delivery and formulation. *Adv Drug Deliv Rev*. **2021**;*175*:113818.
32. Fang YX, Li L, Sui MR, Jiang QZ, Dong N, Shan AS, Jiang JG. Protein transduction system based on tryptophan-zipper against intracellular infections via inhibiting ferroptosis of macrophages. *ACS Nano*. **2023**;*17*:12247–65.
33. Chen WY, Chang HY, Lu JK, Huang YC, Harroun SG, Tseng YT, Li YJ, Huang CC, Chang HT. Self-assembly of antimicrobial peptides on gold nanodots: against multidrug-resistant bacteria and wound-healing application. *Adv Funct Mater*. **2015**;*25*:7189–99.
34. Ong ZY, Gao SJ, Yang YY. Short synthetic β-sheet forming peptide amphiphiles as broad spectrum antimicrobials with antibiofilm and endotoxin neutralizing capabilities. *Adv Funct Mater*. **2013**;*23*:3682–92.
35. Stern D, Cui HG. Crafting polymeric and peptidic hydrogels for improved wound healing. *Adv Healthc Mater*. **2019**;*8*:e1900104.
36. Craik DJ, Fairlie DP, Liras S, Price D. The future of peptide-based drugs. *Chem Biol Drug Des*. **2013**;*81*:136–47.
37. Shao CX, Zhu YJ, Jian Q, Lai ZH, Tan P, Li GY, Shan AS. Cross-strand interaction, central bending, and sequence pattern act as biomodulators of simplified β-hairpin antimicrobial amphiphiles. *Small*. **2021**;*17*:e2003899.
38. Kim W, Zou GJ, Hari TPA, Wilt IK, Zhu WP, Galle N, Faizi HA, Hendricks GL, Tori K, Pan W, Huang XW, Steele AD, Csatary EE, Dekarske MM, Rosen JL, Ribeiro NQ, Lee K, Port J, Fuchs BB, Vlahovska PM, Wuest WM, Gao HJ, Ausubel FM, Mylonakis E. A selective membrane-targeting repurposed antibiotic with activity against persistent methicillin-resistant *Staphylococcus aureus*. *Proc Natl Acad Sci USA*. **2019**;*116*:16529–34.
39. Yang ZY, He SQ, Wei YX, Li XF, Shan AS, Wang JJ. Antimicrobial peptides in combination with citronellal efficiently kills multidrug resistance bacteria. *Phytomedicine*. **2023**;*120*:155070.
40. Lai ZH, Tan P, Zhu YJ, Shao CX, Shan AS, Li L. Highly stabilized α-helical coiled coils kill gram-negative bacteria by multi-complementary mechanisms under acidic condition. *ACS Appl Mater Interfaces*. **2019**;*11*:22113–28.
41. Tan P, Lai ZH, Jian Q, Shao CX, Zhu YJ, Li GY, Shan AS. Design of heptad repeat amphiphiles based on database filtering and structure-function relationships to combat drug-resistant fungi and biofilms. *ACS Appl Mater Interfaces*. **2020**;*12*:2129–44.
42. Bai YS, Meng QW, Wang C, Ma KD, Li JB, Li JP, Shan AS. Gut Microbiota mediates *Lactobacillus rhamnosus GG* alleviation of deoxynivalenol-induced anorexia. *J Agric Food Chem*. **2023**;*71*:8164–81.
43. Li JZ, Li QK, Wu QH, Gao N, Wang ZH, Yang Y, Shan AS. Exopolysaccharides of lactobacillus rhamnosus GG ameliorate salmonella typhimurium-induced intestinal inflammation via the TLR4/NF-κB/MAPK pathway. *J Anim Sci Biotechnol*. **2023**;*14*:23.
44. Song MR, Liu Y, Huang XY, Ding SY, Wang Y, Shen JZ, Zhu K. A broad-spectrum antibiotic adjuvant reverses multidrug-resistant gram-negative pathogens. *Nat Microbiol*. **2020**;*5*:1040–50.
45. Wang YC, Kadiyala U, Qu ZB, Elvati P, Altheim C, Kotov NA, Violi A, VanEpps JS. Anti-biofilm activity of graphene quantum dots via self-assembly with bacterial amyloid proteins. *ACS Nano*. **2019**;*13*:4278–89.
46. Chen TT, Lyu YF, Tan MS, Yang CY, Li Y, Shao CX, Zhu YJ, Shan AS. Fabrication of supramolecular antibacterial nanofibers with membrane-disruptive mechanism. *J Med Chem*. **2022**;*65*:888.
47. Glossop HD, de Zoysa GH, Hemar Y, Cardoso P, Wang K, Lu J, Valéry C, Sarojini V. Battacin-inspired ultrashort peptides: nanostructure analysis and antimicrobial activity. *Biomacromol*. **2019**;*20*:2515–29.
48. Kurnaz LB, Luo YY, Yang XM, Alabresm A, Leighton R, Kumar R, Hwang J, Decho AW, Nagarkatti P, Nagarkatti M, Tang CB. Facial amphiphilicity index correlating chemical structures with antimicrobial efficacy. *Bioact Mater*. **2023**;*20*:519–27.
49. Li QK, Li JZ, Yu WK, Wang ZH, Li JW, Feng XJ, Wang JJ, Shan AS. De novo design of a pH-triggered self-assembled β-hairpin

nanopeptide with the dual biological functions for antibacterial and entrapment. *J Nanobiotechnology*. **2021**;*19*:183.
50. Singh P, Brar SK, Bajaj M, Narang N, Mithu VS, Katare OP, Wangoo N, Sharma RK. Self-assembly of aromatic α-amino acids into amyloid inspired nano/micro scaled architects. *Mater Sci Eng C Mater Biol Appl*. **2017**;*72*:590–600.
51. Ge CL, Zhu JL, Ye H, Wei YS, Lei YH, Zhou RX, Song ZY, Yin LC. Rational construction of protein-mimetic nano-switch systems based on secondary structure transitions of synthetic polypeptides. *J Am Chem Soc*. **2023**;*145*:11206–14.
52. Fielden SDP, Derry MJ, Miller AJ, Topham PD, O'Reilly RK. Triggered polymersome fusion. *J Am Chem Soc*. **2023**;*145*:5824–33.
53. Nandi N, Gayen K, Ghosh S, Bhunia D, Kirkham S, Sen SK, Ghosh S, Hamley IW, Banerjee A. Amphiphilic peptide-based supramolecular, noncytotoxic, stimuli-responsive hydrogels with antibacterial activity. *Biomacromol*. **2017**;*18*:3621–9.
54. Lombardi L, Shi YJ, Falanga A, Galdiero E, de Alteriis E, Franci G, Chourpa I, Azevedo HS, Galdiero S. Enhancing the potency of antimicrobial peptides through molecular engineering and self-assembly. *Biomacromol*. **2019**;*20*:1362–74.
55. Dou XJ, Zhu X, Wang JJ, Dong N, Shan AS. Novel design of heptad amphiphiles to enhance cell selectivity, salt resistance, antibiofilm properties and their membrane-disruptive mechanism. *J Med Chem*. **2017**;*60*:2257–70.
56. Zhao W, Róg T, Gurtovenko AA, Vattulainen I, Karttunen M. Role of phosphatidylglycerols in the stability of bacterial membranes. *Biochimie*. **2008**;*90*:930–8.
57. Cartron ML, England SR, Chiriac AI, Josten M, Turner R, Rauter Y, Hurd A, Sahl HG, Jones S, Foster SJ. Bactericidal activity of the human skin fatty acid cis-6-hexadecanoic acid on *Staphylococcus aureus*. *Antimicrob Agents Chemother*. **2014**;*58*:3599–609.
58. Saeloh D, Tipmanee V, Jim KK, Dekker MP, Bitter W, Voravuthikunchai SP, Wenzel M, Hamoen LW. The novel antibiotic rhodomyrtone traps membrane proteins in vesicles with increased fluidity. *PLoS Pathog*. **2018**;*14*:e1006876.
59. Parasassi T, Di Stefano M, Loiero M, Ravagnan G, Gratton E. Influence of cholesterol on phospholipid bilayers phase domains as detected by laurdan fluorescence. *Biophys J*. **1994**;*66*:120–32.
60. Gong HN, Hu XZ, Liao MR, Fa K, Ciumac D, Clifton LA, Sani MA, King SM, Maestro A, Separovic F, Waigh TA, Xu H, McBain AJ, Lu JR. Structural disruptions of the outer membranes of gram-negative bacteria by rationally designed amphiphilic antimicrobial peptides. *ACS Appl Mater Interfaces*. **2021**;*13*:16062–74.
61. Epand RM, Walker C, Epand RF, Magarvey NA. Molecular mechanisms of membrane targeting antibiotics. *Biochim Biophys Acta*. **2016**;*1858*:980–7.
62. Jin JC, Wu XJ, Xu J, Wang BB, Jiang FL, Liu Y. Ultrasmall silver nanoclusters: highly efficient antibacterial activity and their mechanisms. *Biomater Sci*. **2017**;*5*:247–57.
63. Lam SJ, O'Brien-Simpson NM, Pantarat N, Sulistio A, Wong EH, Chen YY, Lenzo JC, Holden JA, Blencowe A, Reynolds EC, Qiao GG. Combating multidrug-resistant Gram-negative bacteria with structurally nanoengineered antimicrobial peptide polymers. *Nat Microbiol*. **2016**;*1*:16162.
64. Engelberg Y, Landau M. The Human LL-37(17–29) antimicrobial peptide reveals a functional supramolecular structure. *Nat Commun*. **2020**;*11*:3894.
65. Fan Y, Li XD, He PP, Hu XX, Zhang K, Fan JQ, Yang PP, Zheng HY, Tian W, Chen ZM, Ji L, Wang H, Wang L. A biomimetic peptide recognizes and traps bacteria in vivo as human defensin-6. *Sci Adv*. **2020**;*6*:eaaz4767.
66. Cao JW, Xu R, Geng Y, Xu SW, Guo MY. Exposure to polystyrene microplastics triggers lung injury via targeting toll-like receptor 2 and activation of the NF-κB signal in mice. *Environ Pollut*. **2023**;*320*:121068.
67. Wang FH, Zhang QR, Cui J, Bao BW, Deng X, Liu L, Guo MY. Polystyrene microplastics induce endoplasmic reticulum stress, apoptosis and inflammation by disrupting the gut microbiota in carp intestines. *Environ Pollut*. **2023**;*323*:121233.
68. Cai L, Zhu XY, Ruan HJ, Yang J, Wei W, Wu Y, Zhou LZ, Jiang HJ, Ji MH, Chen J. Curcumin-stabilized silver nanoparticles encapsulated in biocompatible electrospun nanofibrous scaffold for sustained eradication of drug-resistant bacteria. *J Hazard Mater*. **2023**;*452*:131290.
69. Sun TT, Liu XS, Su YZ, Wang ZH, Cheng BJ, Dong N, Wang JJ, Shan AS. The efficacy of anti-proteolytic peptide R7I in intestinal inflammation, function, microbiota, and metabolites by multi-omics analysis in murine bacterial enteritis. *Bioeng Transl Med*. **2023**;*8*:e10446.
70. Zheng KY, Setyawati MI, Lim TP, Leong DT, Xie JP. Antimicrobial cluster bombs: silver nanoclusters packed with daptomycin. *ACS Nano*. **2016**;*10*:7934–42.